Department of Precision and Microsystems Engineering

Topology Optimization of Flow-Disrupting Structures Using a Vorticity Objective to Enhance Heat Transfer Coefficient

Floris Marien de Vries

Report no	:2026.005
Coach	:Dr. ir. L. F. P. Noël
Professor	:Prof. dr. ir. M. Langelaar
Specialisation	:Computational Design and Engineering
Type of report	:MSc. Thesis
Date	:January 30, 2026

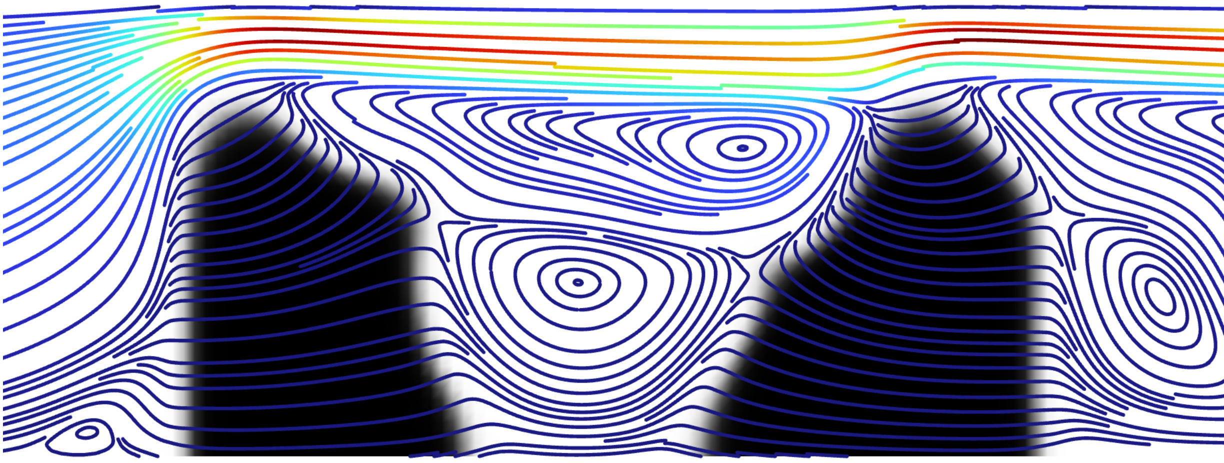

TU Delft Delft University of Technology

ASML

Challenge the future

Topology Optimization of Flow-Disrupting Structures Using a Vorticity Objective to Enhance Heat Transfer Coefficient

by

F.M. de Vries

to obtain the degree of Master of Science
at the Delft University of Technology,

Student number:	4957687	
Project duration:	March 1, 2025 – January 30, 2026	
Thesis committee:	Prof. dr. ir. M. Langelaar,	TU Delft, supervisor
	Dr. ir. L. F. P. Noël,	TU Delft, supervisor
	Dr. C. M. de Servi	TU Delft
	Dr. ir. M. J. B. Theulings	TU Delft
	Dr. ir. S. Gielen	ASML
Company supervisor:	Ir. C. Tümer	ASML

TU Delft

Abstract

This thesis presents a comprehensive investigation into the use of density-based topology optimization (TO) for designing flow-disrupting wall structures that enhance heat transfer in laminar cooling channels. The work is motivated by increasing thermal demands in high-tech machinery, where rising actuator power leads to higher heat loads and necessitates improved convective cooling performance. Because the flow structures inside a channel strongly influence the convective heat transfer coefficient (HTC), this study aims to discover geometries that maximize HTC without relying on predefined shapes.

A Darcy–Forchheimer penalization model is adopted to represent solid regions within the incompressible Navier–Stokes equations, providing a stable optimization process across a range of laminar Reynolds numbers. To avoid the non-physical intermediate densities that arise in conjugate heat-transfer formulations, the thesis introduces a vorticity-based objective function. Based on prior studies linking vorticity to HTC, this objective enables optimization using only the flow model, thereby preventing regions with enhanced heat transfer through gray regions. A preliminary comparison shows that, despite the limitation of not directly considering the temperature problem, the vorticity-based objective yields clearer and more physically meaningful structures than the temperature-based approach.

A set of optimizations is performed across multiple Reynolds numbers and pressure-drop constraints. The resulting designs consistently feature families of rounded triangular structures that increase in height, width, and number as more pressure drop is allowed. Although these structures effectively generate localized vorticity and modify the flow field, a detailed post-processing study using a conjugate heat-transfer model shows that the global thermal performance depends primarily on the allowed pressure drop rather than the precise internal geometry. Parametrized versions of the optimized structures, constructed from averaged geometric features, as well as designs in which the channel is locally narrowed by a single large rectangular obstruction, exhibit nearly identical HTC–pressure-drop relationships. This indicates that, under the conditions considered in this study, the observed increase in HTC is mainly driven by the higher flow velocities induced by channel constriction, rather than by geometry-specific flow features.

The findings indicate that, within the investigated laminar regime and two-dimensional modeling assumptions, the different geometric configurations offer similar thermal–hydraulic performance. The thesis concludes with recommendations for future work, incorporating turbulence models, and exploring three-dimensional designs where geometry-induced mixing may have a stronger effect on heat-transfer enhancement. In addition, future work should consider alternative formulations of the optimization problem that allow for more design freedom, rather than restricting solid structures to a single channel wall.

Contents

1

Introduction

High-tech machinery increasingly demands higher output and greater precision, pushing critical components to operate at increased velocities and accelerations. These requirements place greater power demands on the drive motors, resulting in increased heat generation. Because these motors have a limited operating temperature, effective thermal management becomes essential. Improving the thermal performance of heat exchangers used for active cooling is therefore a key challenge.

The single-flow heat exchangers considered in this study operate by passing a coolant through microchannels adjacent to the heat-generating components. The thermal performance of these channels is determined by reducing the temperature difference between the coolant inlet temperature and the maximum temperature of the heat source. It can be characterized in terms of thermal resistance, which consists of three components: conduction, convection, and caloric resistance. In Figure 1.1, an overview of the three temperature differences is presented, assuming a fully developed flow and thermal boundary layer within the channel. Since this study does not focus on the materials of the heat source, channel wall, or cooling fluid, the conductive and caloric temperature differences are considered fixed. The focus will therefore lie on minimizing the convective thermal resistance by increasing the heat transfer coefficient (HTC). This coefficient strongly depends on the flow profiles within the fluid, which in turn are influenced by the geometry of the flow channels. Consequently, optimizing the channel geometry is essential to improve the performance of the heat exchangers.

An effective approach to increase the HTC is to add geometrical structures to the channel walls that disrupt the flow. These structures create vortices that enhance mixing and disturb the boundary layer, thereby increasing thermal performance. Lemenand et al. (2018) demonstrated the relationship between vorticity and the HTC for vortex generators in a channel. They showed a clear correlation between increased vorticity and improved heat transfer, although the relationship is not perfect as it depends strongly on the specific vortex patterns formed in the flow. The shape of the structures has a significant impact on performance. For example, Ramadhan et al. (2013) and Kumar (2019) studied the influence of various geometric parameters, while Sanhueza and Peeters (2025) applied gradient-based optimization to dimpled plate structures, demonstrating how small geometric perturbations can influence convective performance.

The aforementioned studies all require an initial design to perform parameter or shape optimization, which inherently limits the design space. In this thesis, density-based topology optimization (TO) is used to design wall structures in flow channels without relying on an initial geometry. This technique allows for changing the topology of a certain structure by adding and removing features in the design. Borrvall and Petersson (2003) established the foundation for TO in flow-related problems, and Gersborg-Hansen et al. (2005) extended this method to the Navier–Stokes equations. The density-based method, as introduced by Borrvall and Petersson (2003), employs a Darcy penalization factor to restrict flow through solid regions. Determining the appropriate penalization value is often heuristic, as discussed by Alexandersen (2023). Theulings et al. (2025) proposed a more systematic approach, linking the penalization parameters to material properties and mesh size. This work also introduced

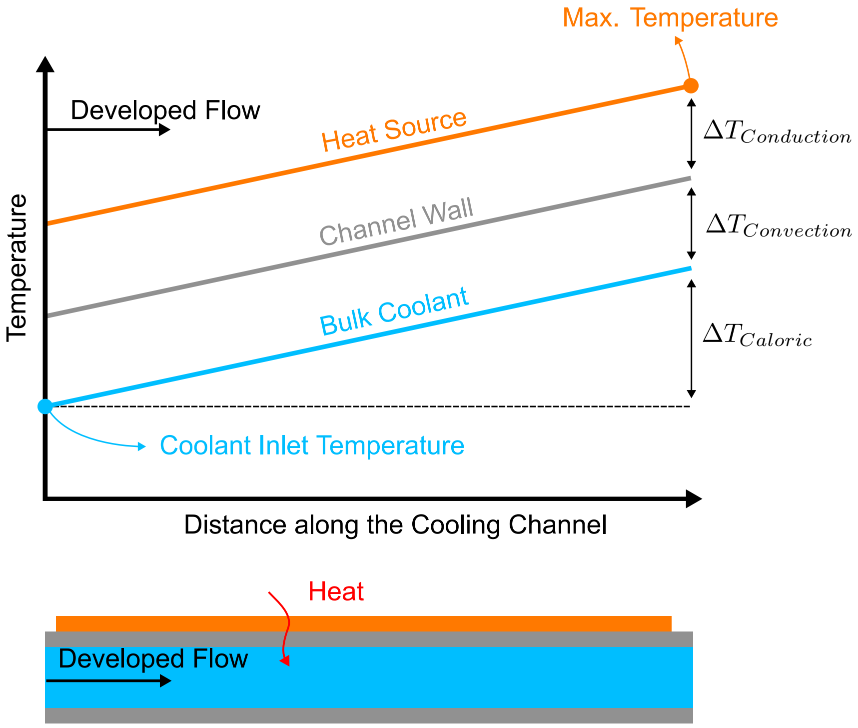

Figure 1.1: Visualization of the temperature differences in a cooling channel. The difference between the coolant inlet temperature and the maximum temperature of the component producing the heat is determined by three components of the thermal resistance.

an additional Forchheimer penalization term, previously used by Philippi and Jin (2015) and Li et al. (2025). The flow penalization approach from Theulings et al. (2025) will be adopted in this thesis.

Dede (2009) was among the first to apply the density-based method to a multiphysics problem involving both fluid flow and heat transfer. Since then, this approach has been widely used to optimize two-dimensional flow channel patterns in heat exchangers (e.g., Zhao et al. (2018), Subramaniam et al. (2019)). However, the accuracy of two-dimensional models is debatable in terms of thermal performance. As shown by Mori and Nakayama (1967) and Arvanitis et al. (2018), the HTC improves significantly due to three-dimensional flow phenomena induced by bends in the channels, effects that two-dimensional models cannot capture. Although TO of three-dimensional models has been investigated (e.g., Dilgen et al. (2018), Rogié and Andreasen (2023)), such studies require substantial computational resources. Therefore, this thesis focuses on optimizing a two-dimensional slice of a straight channel to reduce computational costs while avoiding the inaccuracies associated with modeling two-dimensional bends. Another common issue in density-based optimization for convective heat transfer is the emergence of non-physical gray regions, materials with intermediate properties between solid and fluid. These regions unrealistically combine convective and conductive heat transfer, leading to artificially improved performance.

The goal of this thesis is to use TO to determine optimized wall structures in flow channels that maximize the HTC under various flow conditions and pressure drops. To achieve this goal, a reliable TO framework is required. This thesis explores the use of a vorticity-based objective function to eliminate the need for a heat transfer model during optimization. While the relation between vorticity and HTC is not exact, especially downstream of vortex-generating structures, it is considered sufficiently robust to serve as an objective. Additionally, methods to prevent the formation of floating solid regions are investigated, as the focus is on wall-attached structures that are physically manufacturable.

A recurring challenge for engineers using TO is the loss of intuitive understanding of the resulting designs. Engineers seek not only optimal solutions but also insight into the design rationale. By optimizing for a range of flow conditions rather than a single case, it becomes possible to compare designs and analyze how they evolve under different flow regimes, thereby improving the engineering intuition behind the results. The flow conditions will be varied by changing the Reynolds number while remaining within the laminar regime. This is because most micro-cooling channels in the high-tech industry work with laminar flow; besides, it saves computational cost and is more stable during optimization. After optimization, the resulting designs are converted into more regular geometries using repeated structures defined by a set of geometric parameters. This step enhances manufacturability and increases the interpretability of the structural features.

Based on the objectives described above, the following research question is formulated:

- *What are the optimal wall structures inside a flow channel under various flow conditions that maximize the heat transfer coefficient?*

This leads to the following subquestions:

- *What is an effective flow penalization method for accurately modeling the flow field and maintaining stability at relatively high laminar Reynolds numbers?*
- *To what extent can vorticity be a substitute for a thermal objective when optimizing for heat transfer coefficient?*
- *How can solid structures be constrained to remain attached to the channel wall, considering manufacturability?*
- *Can different optimized designs be interpreted to identify trends and characteristics across various input conditions?*
- *To what extent can the optimized designs be defined by a set of geometrical parameters and show similar performance?*

In Chapter 2, the TO framework is presented, including the Darcy–Forchheimer penalization and the interpolation of penalization value from the design variable. The optimization problem is then formulated, including objectives and constraints. Chapter 3 presents a preliminary study of the performance of the TO method, including a mesh convergence analysis and a comparison between vorticity- and temperature-based objectives. With the final optimization setup established, Chapter 4 discusses the optimized designs obtained under different flow conditions and analyzes the differences between them. A final performance analysis is done comparing all designs. Finally, Chapter 5 summarizes the findings and provides recommendations for future research.

2

Flow model and penalization method for topology optimization

In this chapter, the finite element flow model is introduced together with the penalization method used for TO. First, the governing equations for the flow and heat transfer are presented. These equations are then adapted to incorporate the Darcy–Forchheimer penalization model. The interpolation of the penalization and thermal conductivity from the design variable is explained, along with the filter and projection applied to this variable. Finally, the full optimization problem is formulated, including the definitions of the objectives and constraints.

2.1. Governing equations

In this thesis, a two-dimensional fluid flow model is used with the incompressible Navier-Stokes equations, which take the form:

$$\rho(\mathbf{u} \cdot \nabla)\mathbf{u} = -\nabla p + \nabla \cdot \mu(\nabla \mathbf{u} + (\nabla \mathbf{u})^T) + \mathbf{f}, \tag{2.1}$$

$$\nabla \cdot \mathbf{u} = 0, \tag{2.2}$$

where ρ is the mass density of the fluid, μ the dynamic viscosity, p the pressure, $\mathbf{u}$ the fluid velocity, and $\mathbf{f}$ the body forces.

For the heat transfer model, two different equations cover the solid and the fluid. The pure conductive heat transfer present in the solid domain is governed by:

$$\nabla \cdot (k_s \nabla T) + Q = 0, \tag{2.3}$$

where T is the temperature, k_s the thermal conductivity of the solid, and Q a heat source. In the fluid, both conductive and convective heat transfer take place:

$$\nabla \cdot (k_f \nabla T) + Q = \rho c_p(\mathbf{u} \cdot \nabla T), \tag{2.4}$$

with the specific heat capacity of the fluid c_p and the conductivity of the fluid k_f. It is assumed that the influence of temperature variations on the flow field is sufficiently small to be neglected. The model is therefore treated as a one-way coupled problem, in which the heat transfer depends on the flow, but the flow does not depend on the temperature field.

The dimensionless numbers relevant for this study are the Reynolds number, Re, and Prandtl number, Pr, defined as:

$$Re = \frac{\rho\, U_{in}\, L}{\mu}, \tag{2.5}$$

$$Pr = \frac{c_p\, \mu}{k_f}, \tag{2.6}$$

where U_{in} is the maximum inlet velocity magnitude and L the inlet height of the channel.

The focus of this study is on maximizing the heat transfer coefficient (HTC) of the cooling channel, which is defined as:

$$HTC = \frac{Q}{A_w(T_\Gamma - T_b)}, \tag{2.7}$$

$$T_b = \frac{\int T\,\mathbf{u}\cdot\mathbf{n}\,dy}{\int \mathbf{u}\cdot\mathbf{n}\,dy}, \tag{2.8}$$

where A_w is the wetting area between the fluid and the solid at the heated channel wall, T_Γ is the temperature of the heated channel wall, and $\mathbf{n}$ is the normal vector parallel to the channel wall. To calculate the fluid bulk temperature T_b, the integral is taken over a certain cross-section in the channel.

2.2. Discretization

The governing equations are discretized using a finite element formulation performed in COMSOL Multiphysics® (2023). Both the solid and fluid domains are discretized using quadrilateral elements, where h is the mesh size and N_e the number of elements. Given the rectangular shape of the domain, the discretization results in uniformly shaped square elements. The flow model uses quadratic interpolation for the velocity and linear interpolation for the pressure. Streamline and crosswind diffusion are enabled to stabilize the finite-element solution by suppressing numerical oscillations in the velocity and pressure fields. The heat transfer equations are discretized using linear quadrilateral elements for both the solid and fluid domains.

2.3. Topology Optimization

In density-based TO of flow, a design variable α takes a value between zero and one for every element. From this design variable, an extra term in the Navier-Stokes equations is interpolated. This extra term depends on the velocity and serves as a body force that penalizes the flow velocity in solid regions. When α is zero, the penalization is maximal, modeling a solid, and when α is one, the penalization is zero, modeling the fluid. When α takes a value in between, the flow is only partly penalized, modeling an unphysical domain which should be prevented as much as possible for the final optimized design. Because the value of the design variable is continuous, a gradient-based algorithm can be used. The penalization method used and the formulation of the optimization problem, including the interpolation of the thermal properties, are discussed in this section.

2.3.1. Darcy-Forchheimer penalization

To penalize the flow in the solid domains, an extra term is added that is interpolated from the design variable α. This thesis follows the penalization approach used by Theulings et al. (2025), which makes use of Darcy-Forchheimer penalization. In this method, a Forchheimer term is added, besides the Darcy term that is widely used in literature, see Alexandersen and Andreasen (2020) and Dbouk (2017). This Forchheimer term depends quadratically on the velocity and is supposed to counteract the inertial terms in the Navier-Stokes equations, which now take the following form:

$$\rho(\mathbf{u}\cdot\nabla)\mathbf{u} = -\nabla p + \nabla\cdot\mu(\nabla\mathbf{u} + (\nabla\mathbf{u})^T) + \mathbf{f} - D(\alpha)\,\mathbf{u} - F(\alpha)\,\|\mathbf{u}\|\,\mathbf{u}, \tag{2.9}$$

$$\nabla\cdot\mathbf{u} = 0, \tag{2.10}$$

where the $D(\alpha)$ is the Darcy term and $F(\alpha)$ the Forchheimer term, both interpolated from the design variable. Theulings et al. (2025) also proposes to use a filtered velocity magnitude in the Forchheimer term, however, during this research, no benefit was found by using this.

The initial design field α_0 is defined as a constant value over the design domain. During this study, an initial design corresponding to a fully fluid channel, with $\alpha_0 = 1$, was found to provide the most stable convergence during optimization.

2.3.2. Interpolation from the design variable

The Darcy and Forchheimer terms are interpolated following a similar function as introduced by Borrvall and Petersson (2003). The solid domain is represented by $\alpha = 0$ and the fluid domain by $\alpha = 1$, resulting in the following interpolation functions:

$$D(\alpha) = \overline{D}\frac{10^{-\hat{q}}(1-\alpha)}{10^{-\hat{q}}+\alpha}, \tag{2.11}$$

$$F(\alpha) = \overline{F}\frac{10^{-\hat{q}}(1-\alpha)}{10^{-\hat{q}}+\alpha}, \tag{2.12}$$

where the parameter $\hat{q}$ determines the convexity of the interpolation function. $\overline{D}$ and $\overline{F}$ represent the maximum Darcy and Forchheimer penalization magnitude, respectively, and are defined following Theulings et al. (2025) as:

$$\overline{D} = 10^{q}\frac{\mu}{h^2}, \tag{2.13}$$

$$\overline{F} = 10^{2q}\frac{\rho}{h}, \tag{2.14}$$

where the parameter q defines the order of magnitude of the maximum penalization. During optimization $\hat{q}$ is kept constant while a continuation procedure is performed on q. By starting with lower values for $\overline{D}$ and $\overline{F}$, the aim is to avoid the convergence to inferior local minima. As q is increased during optimization, the optimizer converges to more clear distinctions between solid and fluid regions.

For the heat transfer model, the thermal conductivity is interpolated from the design variable using SIMP:

$$k(\alpha) = (k_f - k_s)\alpha^{\kappa} + k_s, \tag{2.15}$$

where κ is a parameter controlling the convexity of the interpolation function. In the current model, the heat capacity c_p is not interpolated from the design variable because, in solid regions, the velocity approaches zero, causing the convective term in Eq. 2.4 that contains c_p to also vanish.

2.3.3. Filter and Projection

To prevent checkerboarding, where the final design exhibits alternating solid-fluid element patterns, a density filter is introduced, see Lazarov and Sigmund (2010). This distributes the design variable over a predefined radius. In addition, the filter promotes a minimum length scale in the final optimized design. A PDE filter is used and defined as:

$$-R_f^2 \, \nabla^2 \, \alpha_f + \alpha_f = \alpha, \tag{2.16}$$

where R_f is the filter radius and α_f the new filtered design field.

After filtering, large gray areas between the fluid and solid domains are present. To make clearer boundaries between the domains, a Heaviside projection, as described in Wang et al. (2010), is added in the form:

$$\alpha_\beta = \frac{\tanh(\beta(\alpha_f - \eta)) + \tanh(\beta\eta)}{\tanh(\beta(1-\eta)) + \tanh(\beta\eta)}, \tag{2.17}$$

where α_β is the projected design field, β the projection sharpness, and η the projection threshold. The updated design field α_β is used in the interpolation functions in Eqs. 2.11, 2.12, and 2.15 instead of α.

2.3.4. Optimization problem formulation

In this thesis, the optimization problem considered is formulated as:

$$\begin{aligned} \text{Objective:} \quad & \min_{\boldsymbol{\alpha}} \quad \phi(\boldsymbol{\alpha}), \\ \text{Subject to:} \quad & g_i(\boldsymbol{\alpha}) \leq 0 \quad i = 1, ..., N_g, \\ \text{With:} \quad & 0 \leq \alpha_j \leq 1 \quad j = 1, ..., N_e, \end{aligned} \tag{2.18}$$

with ϕ the objective function, g_i the i-th constraint function, and N_g the number of constraints. To solve the optimization problem, the globally convergent method of moving asymptotes (GCMMA) is used. The standard MMA algorithm was found to exhibit oscillatory behavior during the optimization process. The globally convergent version addresses this issue and provides more stable convergence toward an optimized design. The algorithm performs best when both the objective and the constraints are appropriately scaled as described by Svanberg (2007).

In the present model, two constraints are imposed. The first is a volume constraint, which limits the fraction of the design domain that can be filled by solid material and is defined as follows:

$$g_1(\alpha) = \frac{V(\alpha)}{V_f} - 1 \leq 0, \tag{2.19}$$

where

$$V(\alpha) = \frac{1}{N_e} \sum_{j=1}^{N_e} \alpha_j, \tag{2.20}$$

and V_f is the maximum volume fraction that is allowed to be filled with solid. The second constraint fixes the amount of pressure drop that is allowed and takes the form:

$$g_2(\alpha) = \frac{\Delta p}{\overline{p}} - 1 \leq 0, \tag{2.21}$$

where $\overline{p}$ is the maximum allowed pressure drop and Δp is the difference in pressure between the inlet and outlet.

Two objective functions are considered. The first is the minimization of the average temperature along a specified boundary. As follows from Eq. 2.8, this is directly related to maximizing the HTC, since the problems studied here have a constant flow rate and constant heat flux, which together give a constant bulk temperature T_b. The temperature-based objective is expressed as:

$$\phi_T(\alpha) = \frac{T_\Gamma}{T_0}, \tag{2.22}$$

where T_0 is the inflow temperature of the coolant used here as the reference temperature.

The second objective is based on the vorticity vector, defined as:

$$\boldsymbol{\omega} = \nabla \times \mathbf{u}, \tag{2.23}$$

which is the curl of the velocity field. Vorticity quantifies the local spinning motion of the fluid and is related to the amount of mixing, which in turn affects the HTC. The objective is therefore to maximize the vorticity in a certain domain. The objective takes the following form:

$$\phi_\omega = 1 - \frac{\omega_\Omega}{\omega_0}, \tag{2.24}$$

with ω_Ω the average of the vorticity magnitude over a domain and ω_0 a reference vorticity magnitude.

3

Preliminary study on the topology optimization performance

This chapter presents a performance study on the TO problem for optimizing the flow-disrupting structures in a two-dimensional flow channel. Both a temperature-based objective, minimizing the average temperature at the heated boundary, and a vorticity-based objective, maximizing flow vorticity in selected regions, are considered. The chapter first introduces the test geometry, boundary conditions, and optimization setup. Then, the behavior of the optimization is analyzed by comparing the convergence history and development of the design field. The performance of the designs, optimized with different objectives, is compared in terms of vorticity and temperature. The aim is to identify which objective formulation provides the best optimization process and thermal performance. Finally, mesh convergence studies are performed to select suitable mesh sizes for both optimization and postprocessing, and the element type during postprocessing.

3.1. Performance study for different objective functions

Using density-based TO for conjugate heat transfer problems was found to often converge to designs with a lot of intermediate density values, as will be shown later in this chapter. Since vorticity in the flow is closely linked to high HTC, it is investigated whether it can be used as an objective. This way, the heat transfer model does not have to be used during optimization. First, an optimization is performed by minimizing the average temperature at the top boundary. This highlights the issues that arise when using a conjugate heat transfer model in combination with the density-based model. After that, two possible vorticity-based objectives are presented and compared with the thermal objective.

3.1.1. Geometry and boundary conditions

To evaluate the performance of the optimization problem with different objectives, a test model of a relatively short two-dimensional flow channel is used. The geometry and its boundary conditions are shown in Figure 3.1. The domain Ω_f represents the flow channel where the fluid is present. The channel has an inlet of height L_1 and a total length L_2. A fully developed flow enters from the inlet boundary Γ_i with a maximum velocity U_{in}. No-slip boundary conditions are applied along the channel walls, while a zero-pressure condition is imposed at the outlet Γ_o.

The dark gray channel walls represent the solid domains Ω_s. These regions are included in the heat-transfer model and account only for conductive heat transfer. A heat flux, Q is applied at the top surface of the solid, while the inlet flow enters at a constant temperature T_0.

The central section of the channel, Ω_d, is the design domain for TO and forms part of the fluid domain Ω_f. Within this region, the geometry can be modified. In contrast, the white inlet and outlet sections remain passive fluid areas.

For the pressure drop constraint, Δp can be set equal to the inlet pressure, given the zero-pressure

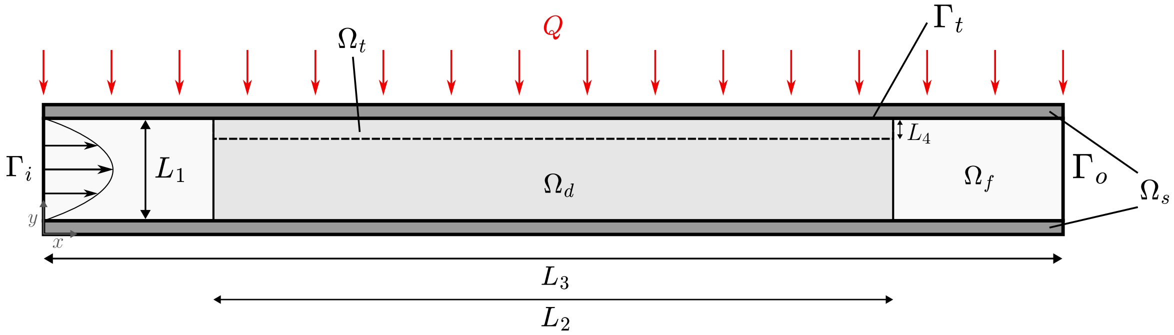

Figure 3.1: Boundary conditions and geometry for flow and heat transfer model

condition at the outlet. The inlet pressure p_{in} is calculated by taking the average pressure over the inlet boundary as follows:

$$\Delta p = p_{in} = \frac{1}{L_1} \int_{\Gamma_i} p \, d\Gamma. \tag{3.1}$$

The maximum allowed pressure drop is computed as:

$$\overline{p} = (L_3 - L_2)\frac{\partial p}{\partial x} + \gamma \, L_2 \frac{\partial p}{\partial x}, \tag{3.2}$$

where

$$\frac{\partial p}{\partial x} = \frac{8 \, \mu \, U_{in}}{L^2}, \tag{3.3}$$

and γ is a parameter multiplying the pressure drop over an empty design domain Ω_d. This parameter controls the maximum allowed pressure drop. The pressure gradient in an empty channel $\partial p/\partial x$ is consistent with Theulings et al. (2025), and is multiplied by the total length of the fluid inlet and outlet regions and by the length of the design domain times the parameter γ.

All parameters and material properties are scaled to be nondimensional and are presented in Table 3.1. The Reynolds number (Re) of 100 is used, and the Prandtl number (Pr) of water is chosen. The ratio between k_f and k_s is based on the ratio between water and stainless steel. During optimization, a continuation is performed on q and β, which are increased every 21 iterations for a total of 147 iterations. The continuation procedure is presented in Table 3.2. The parameter values and continuation scheme were selected to ensure stable convergence of both the flow solver and the adjoint sensitivity solver during optimization for both objectives.

3.1.2. Performance temperature-based objective

The objective is to minimize the average temperature of the top boundary of the fluid domain, T_{Γ_t}. Minimizing this wall temperature is directly linked to increasing the HTC from Eq. 2.8, thereby improving the thermal performance. The optimization result is shown in Figure 3.2, where the filtered and projected design variable α_β is plotted over the design domain. From this figure, the main problem of using a conjugate heat transfer model in combination with the density-based method can be identified. The solution converges to a design containing many intermediate values of α_β, even after the projection. These intermediate values enhance thermal performance because the unphysical intermediate material has both high conduction, allowing heat to flow easily from the boundary into the design domain, and high convection, enabling efficient heat removal by the fluid. It may be possible to prevent this behavior by choosing appropriate penalization and interpolation functions. However, identifying suitable parameter values for a specific problem is a heuristic and often time-consuming process. In this work, a limited number of different parameter choices and modeling approaches were explored, but these did not consistently eliminate the presence of gray regions. For this reason, the focus was shifted toward investigating a vorticity-based objective.

Parameter	Value	Parameter	Value
L_1	1	μ	$\frac{1}{Re}$
L_2	$15L_1$	c_p	$Re\,Pr$
L_3	$10L_1$	T_0	1.7
L_4	$0.2L_3$	Q	1
h	$\frac{L_1}{20}$	V_f	0.4
Re	100	α_0	1
Pr	7	R_f	$2h$
U_{in}	1	η	0.5
ρ	1	γ	60
k_f	1	$\hat{q}$	1
k_s	37	κ	1

Table 3.1: Parameter values during optimization

Iteration	0	21	42	63	84	105	126
q	0	$\frac{1}{3}$	$\frac{2}{3}$	1	$\frac{4}{3}$	$\frac{5}{3}$	2
β	4	4	4	8	8	12	16

Table 3.2: Continuation process

To observe how the objective and constraints evolve during the optimization process, their convergence histories are plotted in Figure 3.3. From the objective history, it can be seen that within one continuation step, the temperature objective decreases, but the overall trend shows a temperature increase. This behavior occurs because the projection sharpness β increases, reducing the number of intermediate values in the design field and thus decreasing thermal performance. As expected, within a continuation step, the vorticity increases when the temperature decreases. In general, vorticity also increases as the projection sharpness increases. This should mean that maximizing vorticity results in clearer designs with fewer intermediate regions.

In the convergence plot of the constraints, the pressure drop constraint becomes active after approximately 45 iterations. The volume constraint becomes active even earlier, but after two continuation steps, the volume fraction suddenly decreases significantly. At this point, the design domain is almost completely filled with intermediate values. However, as the flow penalization factor q increases, material must be removed to maintain the pressure constraint. The same trend continues for the next two continuation steps until β increases, which raises the design values in the solid domains and thus increases the volume fraction.

To compare the performance with the vorticity-based objective, a final design is extracted by applying a threshold value of 0.99 on the design field of α_β. A threshold value of around 0.1 will be used in the next chapter; however, in the present case, this would result in several small solid islands as well as fluid islands surrounded by solid, leading to a relatively complex design. For this reason, a higher threshold value was chosen. For the resulting cutout design, the velocity magnitude is plotted in Figure 3.4.

A performance comparison of key parameters is presented in Table 3.3, where differences are expected due to the choice of threshold value. Although the cutout design shows a similar wall temperature to the initial porous design, the underlying mechanisms are very different. The porous design benefits from the unphysical intermediate material values, while the cutout design relies on increased flow velocity and vorticity. The similarity in wall temperature is therefore likely coincidental. In addition, the cutout design has a significantly lower pressure drop, resulting in better overall thermal–hydraulic performance. At first glance, the lower pressure drop appears counterintuitive, since the porous design allows fluid to pass through the solid region. However, residual penalization in the fluid domain still obstructs the flow and increases the pressure drop. Plots of the vorticity magnitude, temperature, and flow streamlines over the design domain can be found in Figures 3.10a and 3.11a.

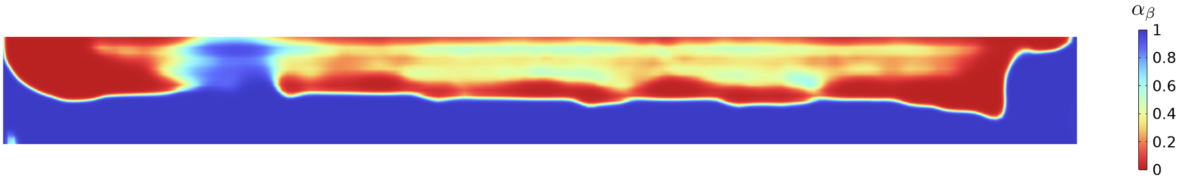

Figure 3.2: α_β over Ω_d optimized by minimizing the temperature of the top boundary

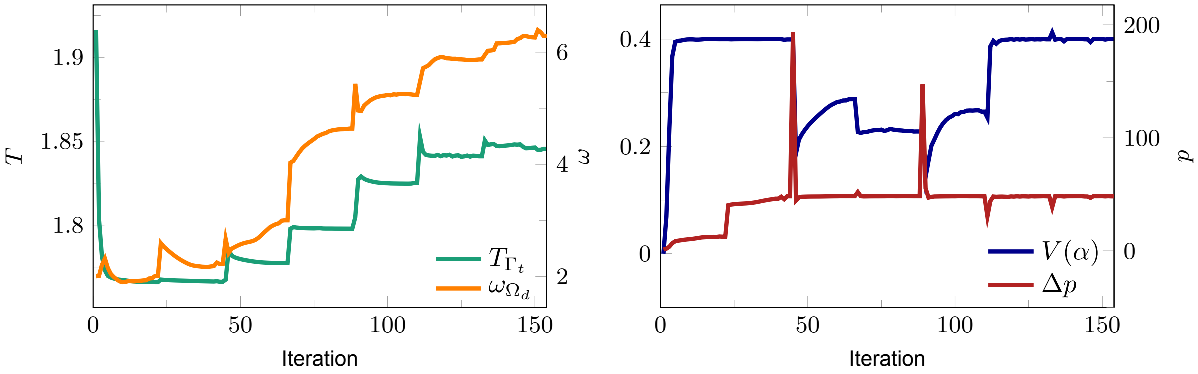

(a) Objectives

(b) Constraints

Figure 3.3: The convergence history of the two possible objectives (a) and the two constraints (b) while using minimization of boundary temperature as the objective

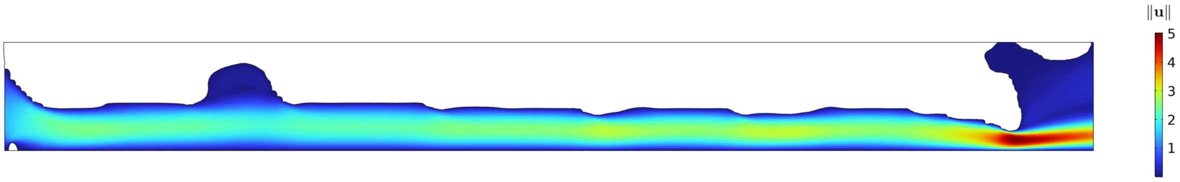

Figure 3.4: Velocity magnitude over the design domain for the cutout design optimized by minimizing the temperature of the top boundary

	Porous design	Cutout design
Δp	48.26	23.84
T_{Γ_t}	1.845	1.873
ω_{Ω_d}	6.286	12.06

Table 3.3: Performance comparison using temperature-based objective

3.1.3. Performance vorticity-based objective

As shown in Figure 3.3, the average vorticity magnitude over the design domain increases as the temperature decreases. Therefore, maximizing vorticity is a promising substitute for a temperature objective. The average vorticity magnitude, ω_{Ω_d}, is calculated as follows:

$$\omega_{\Omega_d} = \frac{1}{L_1 L_2} \int_{\Omega_d} \|\boldsymbol{\omega}\| \, d\Omega, \tag{3.4}$$

and is inserted in the objective equation presented in Eq. 2.24. As a reference value ω_0, the vorticity is taken from a case where the design domain is $\frac{4}{5}$ filled with solid material, forming a large central structure and leaving only the top region Ω_t as fluid. The average vorticity in a two-dimensional channel of height L with a maximum velocity U is given by $2U/L$. In the narrow remaining channel, a fully developed parabolic velocity profile is assumed, for which the maximum velocity is five times higher than U_{in}. Since the channel height is also five times smaller than L_1, the reference vorticity follows as:

$$\omega_0 = 2\,\frac{5\,U_{in}}{\frac{1}{5}\,L_1} = 50\frac{U_{in}}{L_1}. \tag{3.5}$$

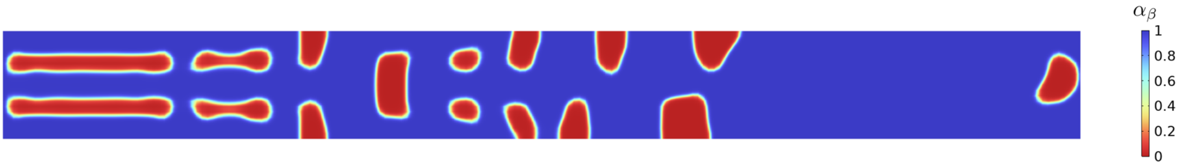

Figure 3.5: α_β over Ω_d optimized by maximizing vorticity over the whole domain as objective

The resulting design field after optimization is shown in Figure 3.5. The boundaries between the solid and fluid regions are much clearer, resulting in fewer intermediate values. However, not all solid regions are connected to the channel wall. In theory, this design could be manufactured by extruding the solid regions in the third dimension; however, because of the small scale of micro channels, making these structures with the correct precision would be associated with excessive manufacturing costs. Since one of the goals of this thesis is to obtain structures connected to the channel walls, a milling constraint was tested as proposed by Høghøj and Träff (2022) and included in the density model of COMSOL Multiphysics. This approach, however, caused instabilities in both the flow solver and the adjoint sensitivity calculations.

Based on the findings in Lemenand et al. (2018), which show that high vorticity near the heated boundary is most important for thermal performance, a solution is proposed. The objective was modified to maximize the average vorticity magnitude in the top domain Ω_t, as presented in Figure 3.1, expressed as:

$$\omega_{\Omega_t} = \frac{1}{L_2 L_4}\int_{\Omega_t} \|\boldsymbol{\omega}\|\, d\Omega. \tag{3.6}$$

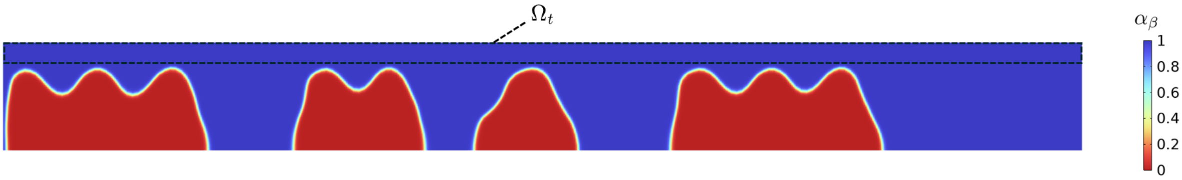

Figure 3.6: α_β over Ω_d optimized by maximizing vorticity over Ω_t as indicated in figure

Using this objective yields the design field shown in Figure 3.6. In this case, the structures are attached to the channel wall without requiring an additional constraint, and the boundaries between solid and fluid regions are clearly defined.

The convergence history for both the objective values and the constraints is shown in Figure 3.7. The vorticity exhibits a similar increasing behavior as seen with the temperature-based objective. The average temperature of the top boundary initially decreases until β increases. As in the previous case, when the amount of intermediate regions decreases, thermal performance declines.

From the constraint convergence plot, the pressure drop constraint becomes active after two continuation steps and remains active thereafter. The volume constraint activates after roughly 10 iterations, but the volume fraction decreases after about 90 iterations. Interestingly, the volume constraint is not active at the end of the optimization. To understand this, the evolution of the design field is examined in Figure 3.8, which shows the design at two different iterations. The optimizer increases vorticity by introducing small wave-like features on top of the structures, achieved by removing some solid material. Although solid material could be added elsewhere, doing so would likely increase the pressure drop. Since the pressure drop constraint is already active, the optimizer avoids adding material.

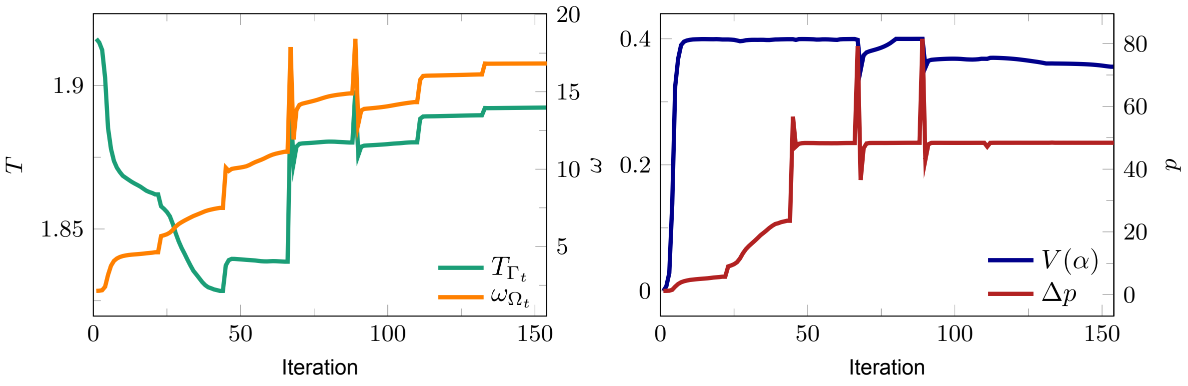

(a) Objectives **(b)** Constraints

Figure 3.7: The convergence history of the two possible objectives (a) and the two constraints (b) while using maximization of vorticity in the top boundary as the objective

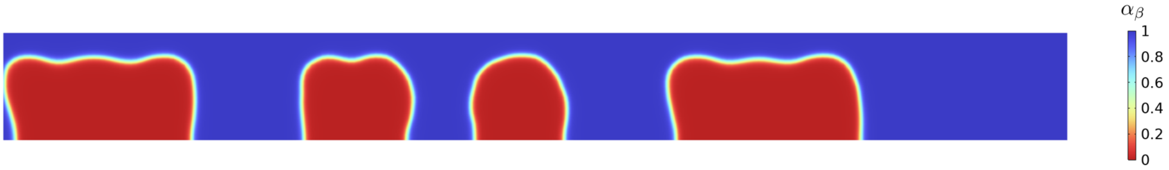

(a) Iteration: 84, $V(\alpha) = 0.40$

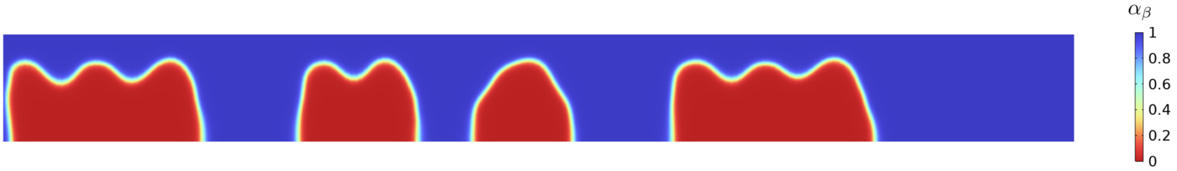

(b) Iteration: 105, $V(\alpha) = 0.36$

Figure 3.8: Design field α_β at two iterations during optimization

As in the previous section, the porous design was converted to a cutout design by applying a threshold value of 0.99 on α_β, to be consistent with the threshold value used for the temperature objective. The velocity magnitude plotted for the cutout design can be found in Figure 3.9. The results are presented in Table 3.4, together with the values for the temperature objective as comparison. Although the pressure drop values are closer, the cutout design still shows a significantly lower pressure drop. Even though the boundaries are more distinct, some penalization remains active in the fluid region, increasing the pressure drop for the porous design. The thermal performance of the cutout design is again similar to the porous design. The vorticity in the top domain is lower for the cutout design because the upper surfaces of the structures lie just below the top domain, meaning that vorticity generated at these boundaries does not contribute to ω_{Ω_t}. However, the overall vorticity across the entire design domain is higher for the cutout design due to the sharper boundaries.

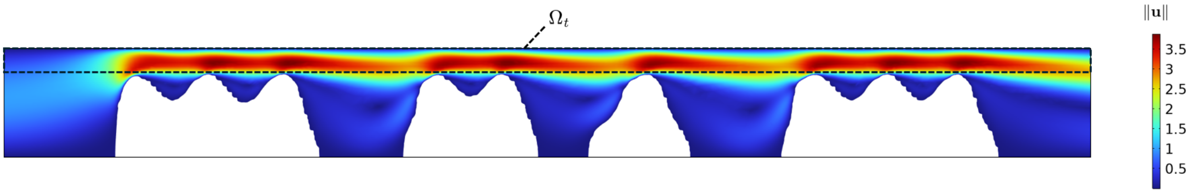

Figure 3.9: Velocity magnitude over the design domain for the cutout design optimized by minimizing the temperature of the top boundary

	Porous design		Cutout design	
Objective	ω_{Ω_t}	T_{Γ_t}	ω_{Ω_t}	T_{Γ_t}
Δp	48.40	48.26	31.19	23.84
T_{Γ_t}	1.892	1.845	1.865	1.873
ω_{Ω_t}	25.25	-	18.90	-
ω_{Ω_d}	7.688	6.29	11.24	12.06

Table 3.4: Performance comparison using vorticity-based objective

3.1.4. Comparison of final designs

Comparing the performance values of the final designs in Table 3.4, it can be seen that the temperature of both cutout designs is very similar, although the pressure drop is lower using a temperature objective, resulting in better thermal-hydraulic performance. This is probably mainly due to the additional contact area between the fluid and the heated boundary, rather than the increase in HTC. The porous design for the vorticity objective represents the final design more accurately. To better understand why the designs perform as they do, the temperature and vorticity profiles across the domain are analyzed.

In Figure 3.10, the vorticity magnitude is shown for both designs. From both designs, it becomes clear that sharp peaks in the geometry result in high vorticity regions, and at the boundaries opposite these peaks, the vorticity is also relatively high. For the structures attached to the top wall, the vorticity near the heated boundary reaches extreme values, while for the structures at the bottom, the vorticity near the heated boundary is more uniform with smaller variations, except for the peak at the end of the domain.

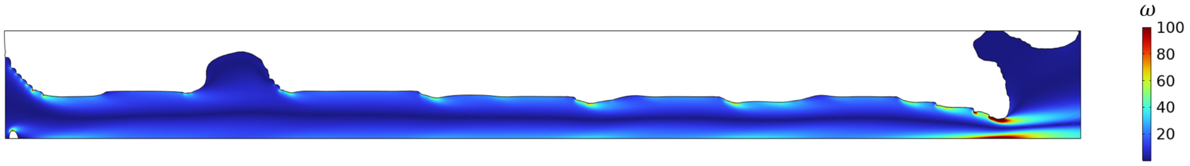

(a) Temperature objective

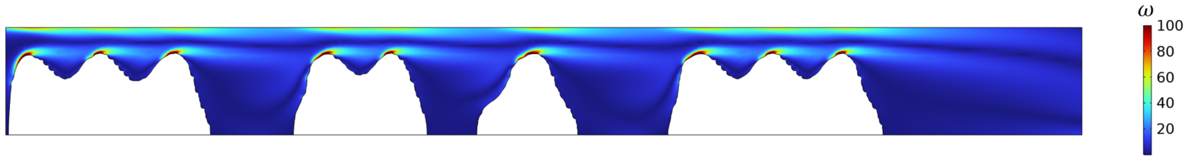

(b) Vorticity objective

Figure 3.10: Vorticity magnitude plotted over design field for both cutout designs

The temperature field and flow streamlines of both designs are shown in Figure 3.11 to further analyze where the thermal performance differences arise. Since the top structures are directly heated, the fluid inside the valleys has a relatively high temperature. From the streamlines, recirculation zones can be identified inside these valleys. These zones involve spinning motion, which slightly increases vorticity, but they are too large to show high vorticity values. Because the fluid circulates within these zones, heat is not effectively removed, causing the fluid to heat up and reducing thermal performance. For the bottom-wall structures, the recirculation occurs away from the heated boundary and therefore has little effect on heat transfer.

From this section, it can be concluded that, although not perfect, vorticity can serve as a reasonable substitute for a temperature-based objective. It is important to note that the comparison between the two objectives in this chapter is not entirely fair. When minimizing the temperature of the top wall, it is expected that most of the solid material will be attached to this wall, whereas the formulation of the vorticity-based objective restricts the design freedom by enforcing attachment of the structures to the bottom wall. This section primarily highlights the difficulties associated with using a temperature-based objective and illustrates how a vorticity-based objective addresses these issues. The restriction of the

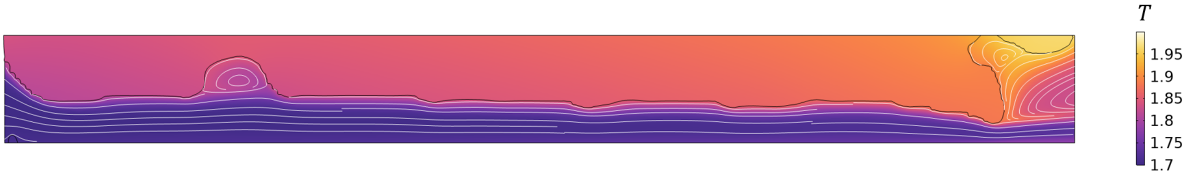

(a) Temperature objective

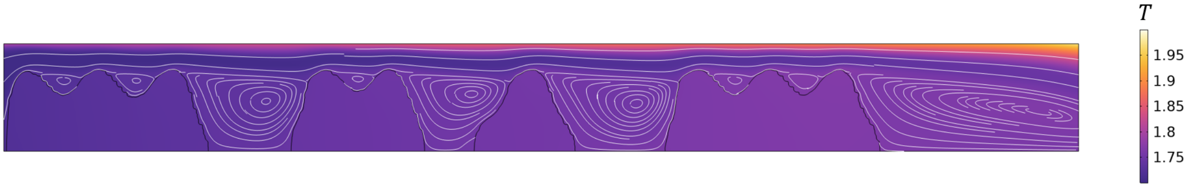

(b) Vorticity objective

Figure 3.11: Temperature plotted over design field for both cutout designs

structures to the bottom wall was subsequently adopted, taking into account manufacturing considerations.

Although the final design performs better using a temperature objective, it is less reliable because of the amount of intermediate region. This means the possibility arises that when changing the flow conditions or pressure drop constraint in the next chapter, designs will perform again very differently. To conclude, the objective in maximizing ω_{Ω_t} will be used for generating the final results in the next chapter.

3.2. Mesh convergence study

To determine an appropriate mesh size for both optimization and post-processing, a mesh convergence study was performed on a reference design. The mesh used in the previous section was relatively coarse to ensure fast optimization runs, which facilitated the trial-and-error process of the development of the final optimization approach. Two element types were considered for post-processing, while the element type used during optimization, rectangular elements, was already fixed. Figure 3.12 shows the geometry of the reference design with the boundary conditions. The model consists of a two-dimensional slice of a rectangular flow channel containing solid structures with rounded edges. These structures are included to replicate the vorticity and HTC patterns expected during optimization. An empty channel would exhibit low vorticity and would not accurately represent the flow profiles in optimized designs. The dimensions and properties of the model, presented in Table 3.5, are chosen to be representative of micro cooling channels used in high-tech industries, using water as a coolant and stainless steel for the solid parts. This design will also be used in the next chapter to compare the performance of the final optimized designs.

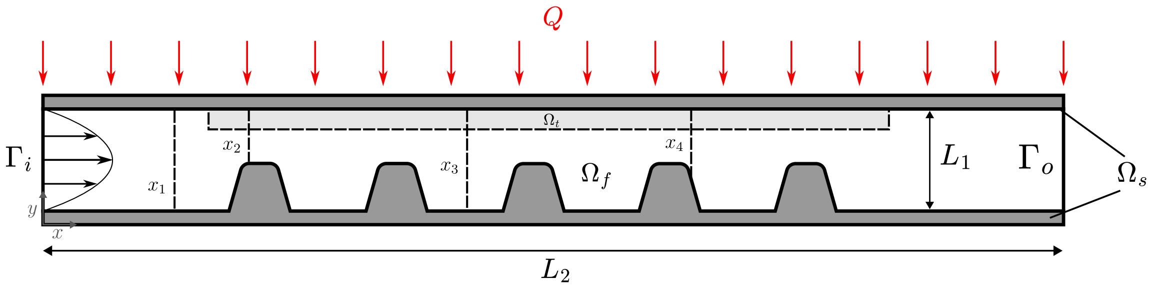

Figure 3.12: Boundary conditions and geometry for reference design used for performing the mesh study

Two different element types were tested in this study: quadrilaterals and triangles. Quadratic interpolation was used for the velocity and linear interpolation for the pressure, consistent with the setup used

Parameter	Value	Unit
L_1	0.001	m
L_2	$15L_1$	m
Q	10000	$W\ m^{-2}$
T_0	300	K
Re	500	
U_{in}	$\frac{Re\ \mu}{\rho\ L_1}$	ms^{-1}
ρ	1000	$kg\ m^{-3}$
μ	0.001	$Pa\ s$
k_f	0.6	$W\ m{-1}\ K^{-1}$
k_s	237	$W\ m{-1}\ K^{-1}$
c_p	4184	$J\ kg^{-1}\ K^{-1}$

Table 3.5: Parameters for the reference model performing the mesh convergence study

during optimization. Figure 3.13 shows an enlarged portion of the channel, highlighting the structure of the two mesh types. For both element types, five quadrilateral boundary layer elements were added along the walls to accurately capture the flow behavior near the boundaries.

Six different mesh sizes, ranging from $\frac{L_1}{10}$ to $\frac{L_1}{100}$, were used to compute the solution. To determine the element type and mesh size during post-processing, the HTC was evaluated at four locations: $x_1 = 1.0 \cdot 10^{-3}$, $x_2 = 4.5 \cdot 10^{-3}$, $x_3 = 7.8 \cdot 10^{-3}$, and $x_4 = 9.3 \cdot 10^{-3}$ meters, as indicated in Figure 3.12. These locations were selected to have variations in mesh structure and flow profile.

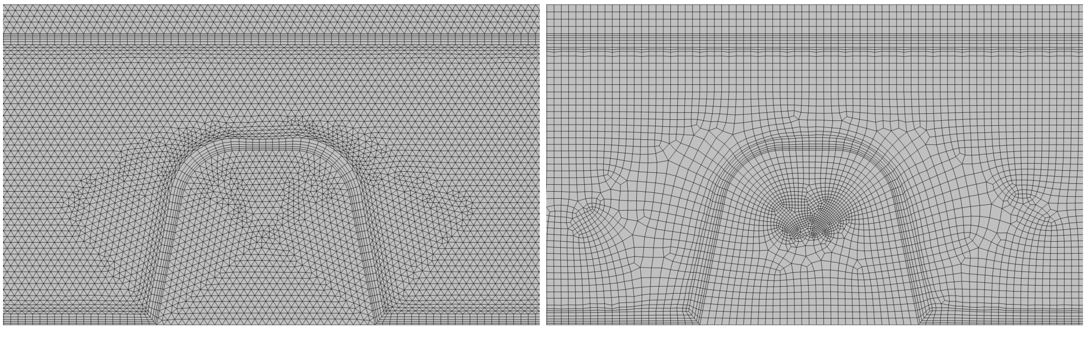
(a)

(b)

Figure 3.13: Close-up of mesh in channel with two different element types of $h = \frac{1}{40}$

Figure 3.14 shows the convergence of the HTC for both element types at the four x-locations. From these results, quadrilateral elements are identified as the more reliable choice. However, triangles are used during post-processing because COMSOL Multiphysics often fails to automatically generate a quadrilateral mesh, and manually constructing such a mesh for every design would be too time-consuming given the number of cases evaluated. A mesh size of $h = \frac{L}{40}$ was selected, as indicated in red in the plots: it is sufficiently close to the converged value while remaining computationally affordable.

To determine the mesh size used during optimization, the vorticity magnitude in the top domain Ω_t, the quantity used in the objective function, is evaluated. The convergence plot of this average vorticity magnitude for both element types, shown in Figure 3.15, confirms that quadrilateral elements are more accurate. As before, a mesh size of $h = \frac{L}{40}$ was selected, as indicated in the figure.

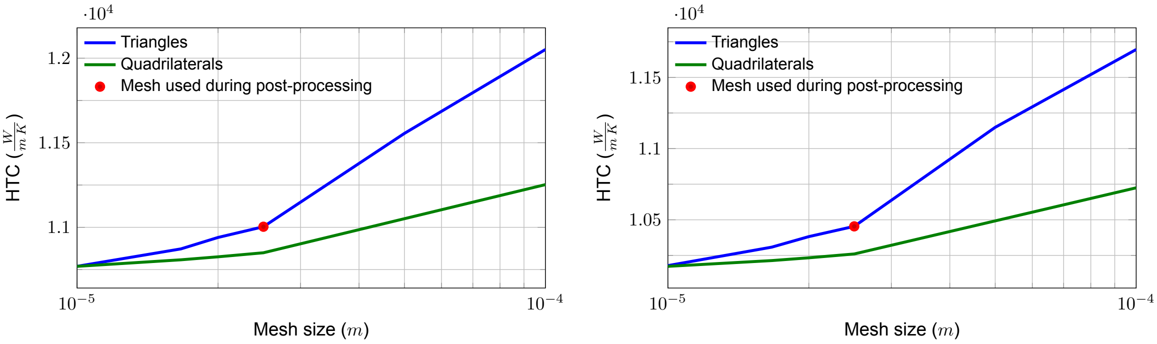

(a) $x_1 = 0.001\ m$ **(b)** $x_1 = 0.0045\ m$

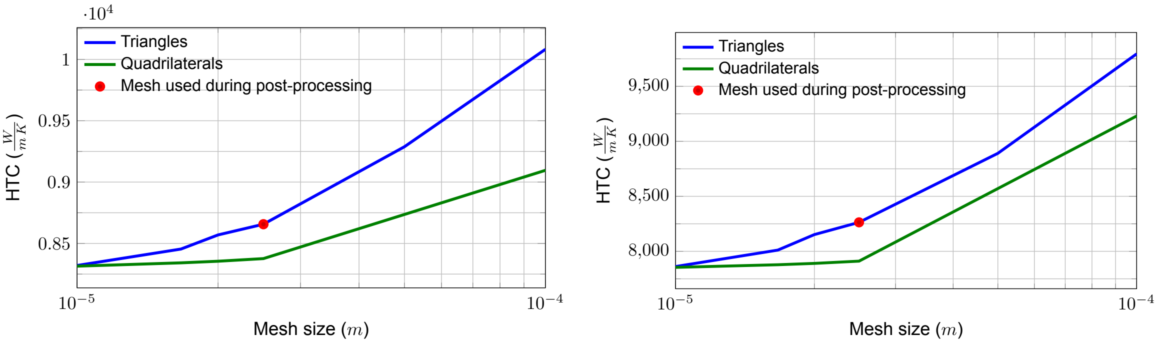

(c) $x_1 = 0.0078\ m$ **(d)** $x_1 = 0.0093\ m$

Figure 3.14: Mesh convergence study on HTC on 4 locations with two different element types

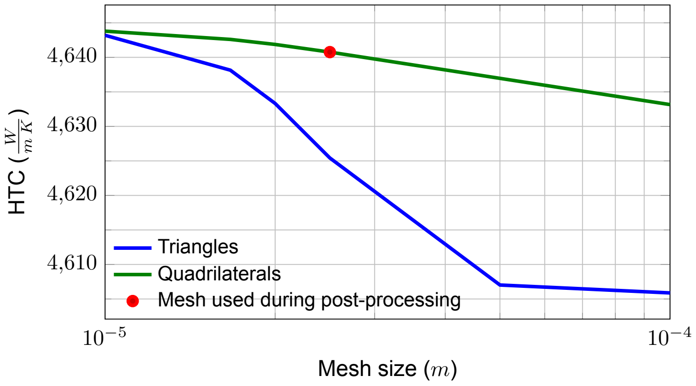

Figure 3.15: Mesh convergence study on ω_{Ω_t} with two different element types

4

Full optimization study and results

This chapter presents the full optimization study and the results of the different optimizations performed under varying flow conditions. First, the values of the input parameters used during optimization and during post-processing are introduced. Next, the performance of the optimized designs is evaluated, and key geometric characteristics are identified. The parameters defining a repeated structure are then extracted from the optimized designs. A performance comparison is made between the optimized designs and the corresponding parametrized designs. Finally, all designs are evaluated over a range of Reynolds numbers to identify the best-performing designs overall.

4.1. Parameter values during optimization and post-processing

The geometry and boundary conditions used in the previous chapter are shown again in Figure 4.1 and are used here for the final optimizations. The only modification is that the channel length is increased to provide more design space for the optimizer, resulting in additional structures over which averages can be taken for the parametrization later on. The input parameters for optimization are listed in the left column of Table 4.1 and remain nondimensional. Because a vorticity-based objective is used, only the fluid flow problem is solved during optimization. The heat flux presented in red is only active during post-processing.

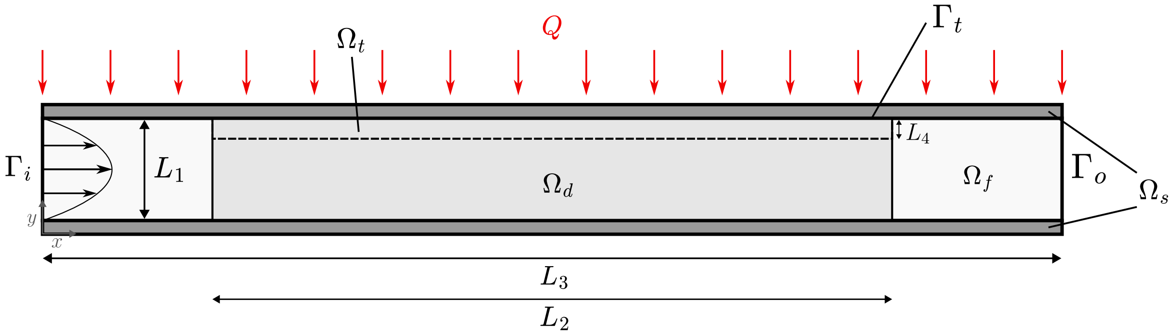

Figure 4.1: Boundary conditions flow model for final topology optimization

The continuation scheme used during optimization differs slightly from that in the test model and is summarized in Table 4.2. The initial projection sharpness β is reduced to improve stability. In addition, three continuation steps are added in which q is held constant while β increases. This adjustment is necessary because simultaneously increasing both q and β up to $\beta = 16$ caused stability issues in the convergence of the flow solver.

Since the objective of this thesis is to evaluate optimized designs under various flow conditions, optimizations are performed for multiple Reynolds numbers and pressure-drop constraints. The initial plan was to investigate values of Re from 100 to 750, but stability problems, discussed in the next section,

Optimization		**Post-processing**		
Parameter	Value	Parameter	Value	Unit
L_1	1	L_1	0.001	m
L_2	$50L_1$	h	$\frac{L_1}{40}$	m
L_3	$\frac{2}{3}L_2$	k_f	0.6	$W\ m^{-1}\ K^{-1}$
L_4	$\frac{1}{5}L_1$	k_s	22	$W\ m^{-1}\ K^{-1}$
h	$\frac{L_1}{40}$	c_p	$4,148$	$J\ kg^{-1}\ K^{-1}$
U_{in}	1	U_{in}	$\frac{Re\ \mu}{L_1\ \rho}$	$m\ s^{-1}$
ρ	1	ρ	$1,000$	$kg\ m^{-3}$
μ	$\frac{1}{Re}$	μ	0.001	$Pa\ s$
V_f	0.4	Q	$10,000$	$W\ m^{-2}$
α_0	1	d	0.001	m
R_f	$2h$			
η	0.5			
$\hat{q}$	1			

Table 4.1: Parameter values during optimization and post-processing.

Iteration	0	21	42	63	84	105	126	147	168	189
q	0	$\frac{1}{3}$	$\frac{2}{3}$	1	$\frac{4}{3}$	$\frac{5}{3}$	2	2	2	2
β	2	2	2	4	4	4	8	8	16	16

Table 4.2: Continuation process

restricted the range up to $Re = 300$. γ ranges from 1 to 600, though the specific values vary depending on the Re. The effect of a given γ is Reynolds-number dependent; for example, achieving a pressure drop corresponding to $\gamma = 300$ is feasible at $Re = 300$, whereas achieving the same pressure drop at $Re = 100$ would require nearly making the entire channel solid, despite the viscosity-dependent definition of the constraint in Eq. 3.1. Consequently, the γ values increase with increasing Re.

The used combinations of Re and γ are listed in Table 4.3, where each combination corresponds to a separate optimization run, giving a total of 25 designs. Only the combinations that did not result in any errors and showed convergence to a final solution are reported.

Re	γ
100	$1.5, 2, 5, 10, 20, 25, 40, 50, 100, 150, 200$
200	$5, 10, 20, 25, 40, 50, 100, 150, 200$
300	$100, 150, 200, 300, 600$

Table 4.3: All combinations of values for Re and γ for the different optimization runs. Every combination of the two parameters being a single optimization

4.1.1. Parameters during post-processing

For evaluating the optimized designs, dimensional parameters are introduced. These parameters approximate micro-cooling channels used in industry, with water as the coolant and stainless steel as the solid channel walls and structures. Since viscosity is fixed during post-processing, the Reynolds number is varied by adjusting the maximum inlet velocity U_{in}. All post-processing parameters are listed in the right column of Table 4.1. An in-plane channel thickness d is used to more accurately compute the pressure drop and heat transfer in the two-dimensional model. A fully developed temperature profile is used at the inlet instead of a constant temperature. This profile is obtained from an empty channel with the dimensions specified in the right column of Table 4.1, with $L_2 = 300L_1$. For all Reynolds numbers, the HTC converges to approximately $1620\frac{W}{m^2\ K}$ at the channel outlet. The thermal entry length is taken as the distance where the HTC reaches 1.05 times the outlet value. For $Re = 100$, this occurs at $x = 0.07\,m$, where the temperature profile presented in Figure 4.2 is obtained. This temperature profile is used for the fluid at the channel inlet during post-processing.

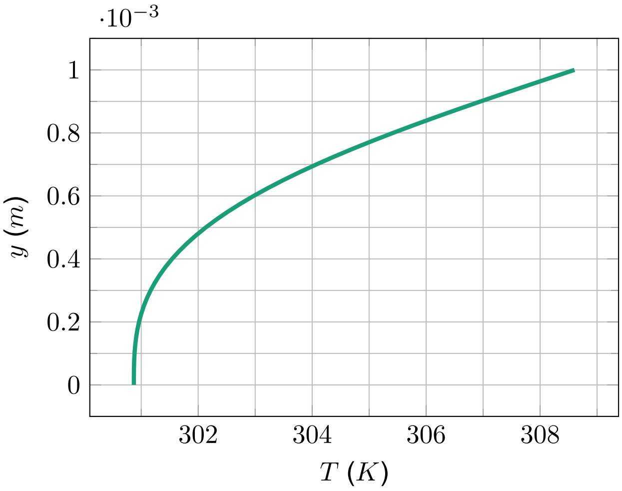

Figure 4.2: Temperature profile of fluid at the inlet of the channel

4.1.2. Stability problems high Reynolds numbers

Higher Reynolds numbers than 300 led to stability issues during optimization, making the resulting designs unreliable. At higher Re, the optimizer attempts to reduce the flow velocity by adding penalization throughout the domain, which artificially lowers the effective Reynolds number. This produces extreme pressure-drop values while the solid structures added to the domain remain relatively small.

A primary cause of the instability is that the spatially varying flow penalization destabilizes the flow solver. The built-in stabilization methods in COMSOL Multiphysics are not designed to handle flow with Darcy–Forchheimer penalization. One potential solution is to include the Darcy–Forchheimer term directly in the stabilization, similar to the approach used in Alexandersen, Aage, et al. (2014) for Darcy penalization. However, COMSOL does not currently allow modification of the stabilization formulations. An attempt was made to implement the stabilization manually, but it was unsuccessful. The procedure followed for this attempt is described in Appendix B.

A second issue is that the added structures locally increase the Reynolds number to the point where the flow would become turbulent, although the laminar flow model can not model this. This means the laminar flow model used during optimization can no longer obtain a solution. Even at $Re = 300$, full optimization runs often required twice the expected computation time due to repeated difficulties solving the flow field. For the cutout design at $Re = 300$, it was already observed that the shear stress transport (SST) turbulence model, see Menter (1994), solved the flow more efficiently than the laminar model. This indicates that for higher Reynolds numbers, it may be necessary to employ a turbulent flow model during optimization.

4.2. Evaluation optimized designs

After completing the optimization runs, the resulting designs were evaluated for both performance and geometry. An overview of all design fields is presented in Appendix A. This section highlights only the most relevant observations. Performance evaluation follows the same procedure as in Chapter 3: each design is converted to a cutout design using a cutoff value of 0.1, unless stated otherwise. The resulting geometry is then scaled by a factor of 0.001 to match the microchannel dimensions, and the parameters listed in the right column of Table 4.1 are applied. After presenting the global performance of the cutout designs, the geometrical characteristics of the optimized structures are examined. Recurring features are identified, analyzed, and accompanied by hypotheses explaining their appearance.

To compare the performance of all designs, the average HTC over the full channel length is evaluated. In Eq. 2.8, T_{Γ_t} is used as the wall temperature. The average bulk temperature is obtained by computing T_b at the inlet and outlet and taking the mean of these two values. For the cases considered here, T_b should remain constant, since the system is in steady state with a constant heat flux and flow rate.

4.2.1. Global performance optimized designs

To assess the global performance, the HTC, the average temperature T_{Γ_t}, and the average vorticity ω_{Ω_t} are plotted against the pressure drop Δp in Figure 4.3. For all three metrics, the global trends with increasing pressure drop behave as expected: the HTC and vorticity increase, while the average temperature decreases.

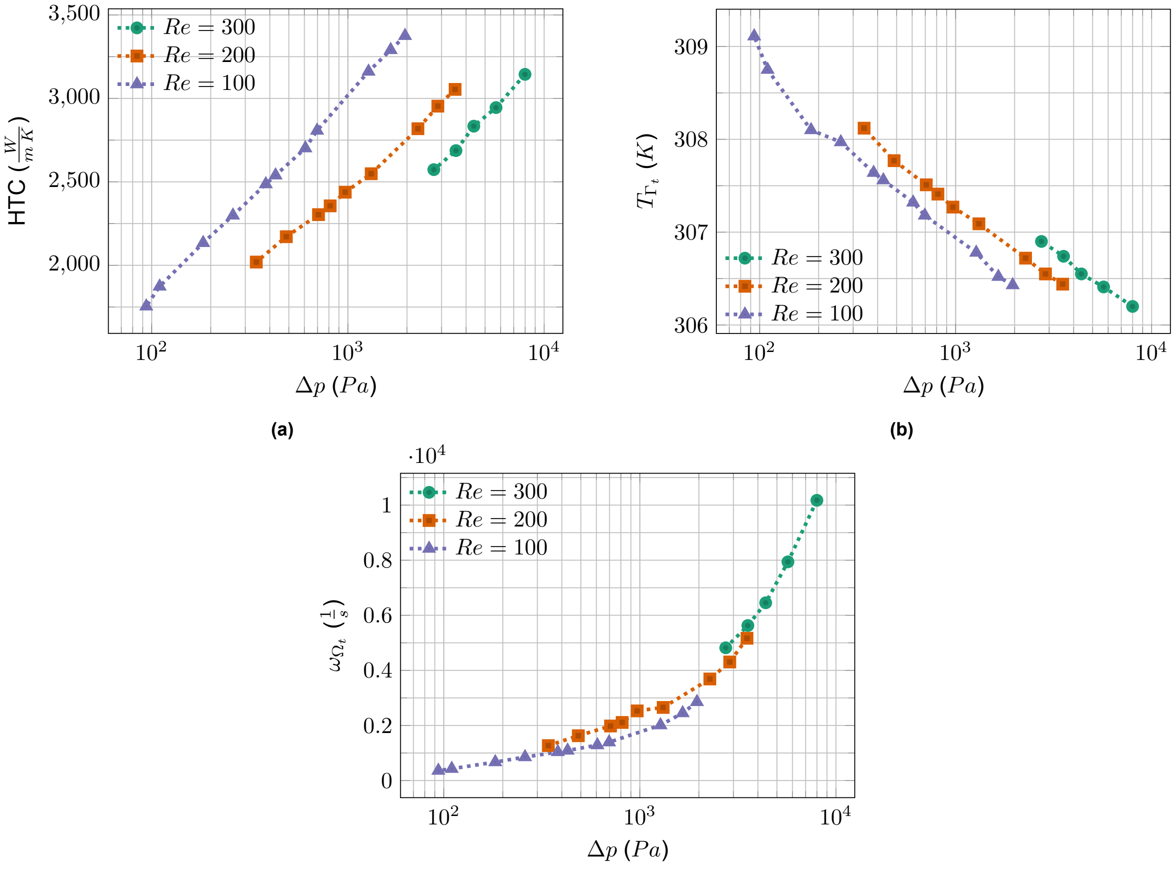

(a)

(b)

(c)

Figure 4.3: Comparison of ω_{Ω_t}, T_{Γ_t}, and HTC vs Δp for all optimized designs.

4.2.2. Geometrical trends in optimized design

To understand which geometric features contribute to the observed performance improvements, the designs were inspected visually. Although Appendix A provides a complete overview, three representative design fields optimized for $Re = 200$ are shown in Figure 4.4. These examples illustrate several trends observed across all optimizations. As the allowable pressure drop increases, more structures appear in the flow channel, and these structures become both taller and wider. This behavior aligns well with physical intuition: a higher pressure drop allows for more and bigger flow-disturbing features.

In all designs, a structure directly attached to the left boundary of the design domain is observed. In flow-related TO problems, it is common for solid material to be placed near the inlet in order to influence the incoming flow. In the present case, a fluid inlet region is still present upstream of the first structure, although this region is not visible in the plots. This inlet region prevents the optimizer from completely blocking the inlet with solid material.

The structure located at the upstream edge of the design domain is, in this case, not only a consequence of the optimization method but also beneficial for thermal performance. By introducing flow guidance and disruption as early as possible, the flow is disrupted over a longer distance. This promotes heat transfer throughout the channel, making upstream flow-disrupting structures more effective than structures introduced further downstream.

It can also be seen that all structures have somewhat the same rounded triangular shape, which can be found in almost all designs. This can indicate that the optimizer prefers narrow peaks to locally increase the vorticity substantially.

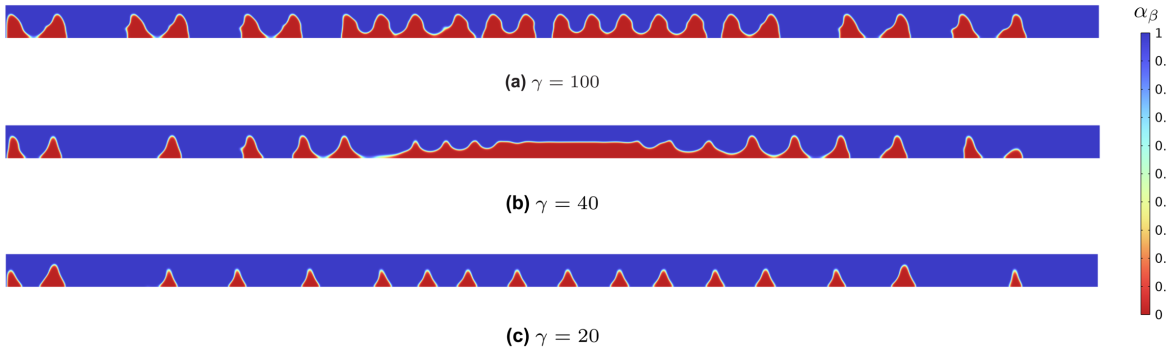

(a) $\gamma = 100$

(b) $\gamma = 40$

(c) $\gamma = 20$

Figure 4.4: The resulting design field of α_β over Ω_d optimized at $Re = 200$ with three different γ

It can be observed that nearly all designs exhibit a similar rounded triangular structure. This recurring shape suggests that the optimizer favors narrow peaks to locally increase both the vorticity and the velocity magnitude. The associated increase in velocity is illustrated in Figure 4.5, where the velocity magnitude is plotted for the cutout designs corresponding to the geometries shown in Figure 4.4. These plots demonstrate that allowing a higher pressure drop leads to larger structures, which reduce the available flow cross-section and consequently increase the flow velocity. This velocity increase contributes substantially to the observed improvement in thermal performance.

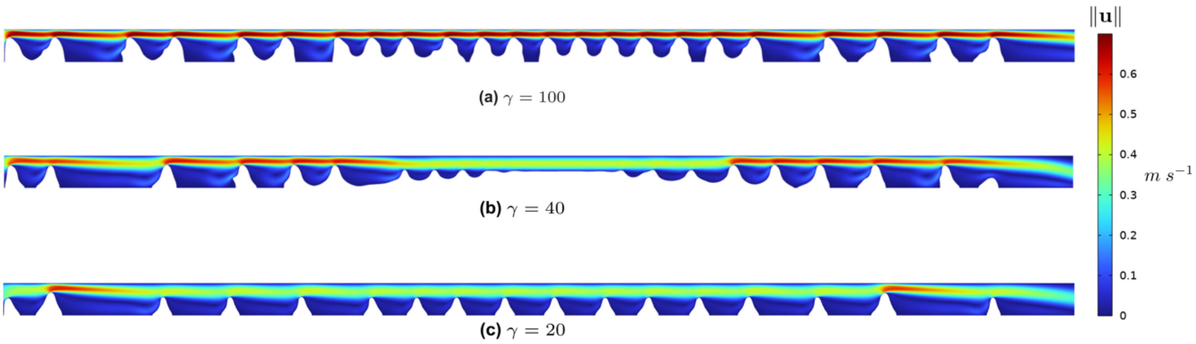

(a) $\gamma = 100$

(b) $\gamma = 40$

(c) $\gamma = 20$

Figure 4.5: The velocity magnitude of cutout designs optimized at $Re = 200$ with three different γ

4.2.3. Convergence to single large structure

Besides the triangular-shaped structures in the design for $\gamma = 40$, a larger structure appears in the middle of the channel. This suggests that the optimizer tends toward forming a narrower channel. Such behavior can be explained by the fact that narrowing the channel increases the flow velocity and therefore the vorticity. A narrow channel also exhibits a higher HTC relative to a wider one. This convergence toward a central structure is seen more frequently in designs optimized for $Re = 100$. This raises the question of whether this single structure or the smaller structures are the preferred design.

To investigate this, additional optimizations were carried out with constant Re and γ, but with varying maximum allowed volume fractions V_f. The resulting designs for $Re = 100$ and $\gamma = 10$ under four different values of V_f are shown in Figure 4.6. As V_f increases, the optimizer consistently produces larger central structures that create a narrow channel. The volume constraint is never active: the total solid volume V remains below V_f for all cases, as was also discussed in Chapter 3. Although the constraint is inactive, V does increase as V_f increases, as listed in Table 4.4.

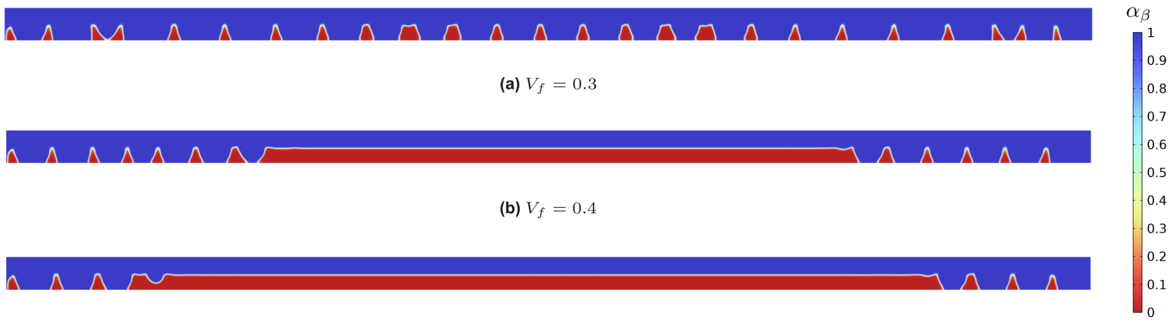

(a) $V_f = 0.3$

(b) $V_f = 0.4$

(c) $V_f = 0.6$

Figure 4.6: The resulting design field of α_β over Ω_d optimized at $Re = 100$ with $\gamma = 10$ for three different volume constraints

The next question is whether this single large structure actually performs better or whether this behavior is a result of the optimization procedure. To test this, the performance of the designs with different volume constraints is evaluated using the cutout geometries and the parameter values from the right column of Table 4.1. Using the standard cutoff value of 0.1 results in different pressure drops between the designs, which does not allow a fair comparison because a higher pressure drop typically leads to a higher HTC. To obtain comparable pressure drops, the cutoff value was adjusted to add or remove material as needed. This way, the height of the structures is a little higher than for the single large structure, increasing the pressure drop to the same value. The results in Table 4.4 show that the HTC values are very close, and the differences are negligible. This indicates that for $Re = 100$, placing a single large structure performs the same as placing multiple smaller structures.

V_f	V	Cutoff value	Δp (Pa)	HTC ($\frac{W}{m\,K}$)	T_{Γ_t} (K)	ω_{Ω_t} ($\frac{1}{s}$)
0.3	0.126	0.03	265.7	2314	307.94	864.6
0.5	0.330	0.1	269.2	2313	307.93	872.2
0.6	0.401	0.2	264.7	2309	307.95	863.1

Table 4.4: Performance of cutout designs optimized with $Re = 100$ and $\gamma = 10$ with three different volume constraint. The cutoff value is varied to have a comparable pressure drop.

A possible explanation is that geometric structures only outperform a narrow channel at higher Re. The motivation for adding such structures is that they disrupt the flow and enhance mixing, increasing the HTC. These flow disturbances arise from inertial effects, which become more dominant at higher Reynolds numbers. Thus, the impact of flow-disturbing structures should be greater at higher Re. To test this hypothesis, a similar study was performed for $Re = 300$ and $\gamma = 300$. The resulting designs for three different values of V_f are shown in Figure 4.7.

These designs show that at $Re = 300$, even at high V_f, the optimizer always adds small patterns in the design to disrupt the flow. The performances of the three designs are compared in Table 4.5. Since the performance values were already very close, the cutoff values were not adjusted. The results again show that the performance of the different designs is very similar. This raises the question of how much the performance relies on specific geometry and if the influence on the thermal performance is due to the disruption of the flow or mainly because of the increase in flow velocity near the top boundary. This will be discussed in Section 4.5.

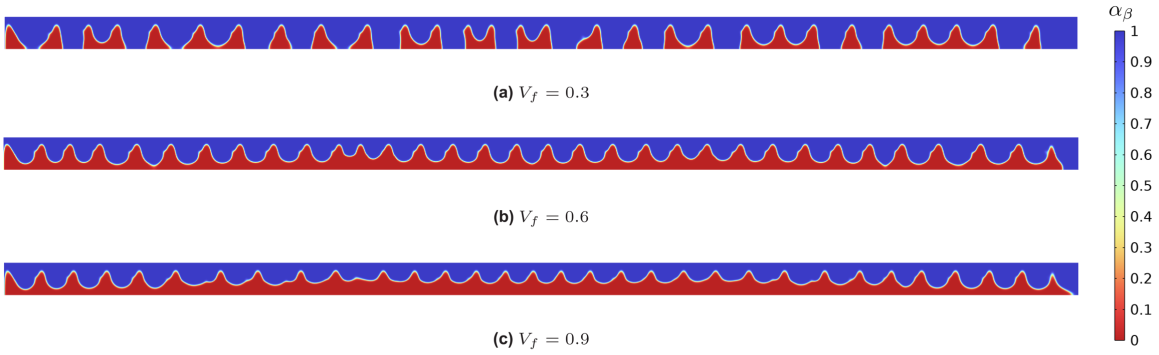

(a) $V_f = 0.3$

(b) $V_f = 0.6$

(c) $V_f = 0.9$

Figure 4.7: The resulting design field of α_β over Ω_d optimized at $Re = 300$ with $\gamma = 300$ for three different volume constraints

V_f	V	Cutoff value	Δp (Pa)	HTC ($\frac{W}{m\,K}$)	T_{Γ_t} (K)	ω_{Ω_t} ($\frac{1}{s}$)
0.3	0.300	0.1	5757	2949	306.41	8041
0.6	0.342	0.1	5616	2925	306.44	7901
0.9	0.500	0.1	5645	2929	306.43	7962

Table 4.5: Performance of cutout designs optimized with $Re = 300$ and $\gamma = 300$ with three different volume constraint.

4.2.4. Local structure geometries

The general shapes of the structures are, in almost all cases, triangular with rounded sides and corners. Between the structures, these curved shapes also help guide the recirculating flow. To illustrate this, flow streamlines for two designs with $Re = 200$ are shown in Figure 4.8 over the upstream $1/5$ of the design domain. The recirculating flow can be seen to follow the boundaries of the structure groups.

A notable feature is the emergence of secondary rounded patterns on the structures, which locally alter the flow profile. For $\gamma = 100$, these secondary patterns are minimal and likely have limited influence. When more pressure drop is allowed, as with $\gamma = 200$, the patterns become more pronounced and begin to split the recirculation zones into upper and lower regions. This behavior likely occurs because the optimizer attempts to approach a design similar to the one in Figure 4.7c, where additional solid material exists between structures and portions of the channel boundary are no longer in direct contact with the fluid. Due to the imposed volume constraint, the optimizer cannot add solid material in these regions. Instead, by introducing secondary patterns, it recreates the flow behavior that would occur if more solid were present.

4.2.5. Discussion on global performance and geometry of designs

The global performance trends in Figure 4.3 indicate that the optimizer consistently uses the additional allowable pressure drop to increase the vorticity. Both vorticity and HTC increase with pressure drop, again highlighting their correlation, although the vorticity rises more rapidly, showing that the relation between the two metrics is not proportional. The analysis of the volume constraint indicates that the specific value of V_f does influence the geometry of the final design, but not its thermal performance.

Several studies on the influence of V_f show that allowing somewhat more solid generally leads to slightly different values of the vorticity objective. The ideal value for V_f differs with the allowable pressure drop. Because of this, it may be preferable to impose a minimum volume constraint with a relatively low value, giving the optimizer more design freedom. This approach is not explored further in this thesis, but Appendix B provides an example of an optimization run using a minimum volume constraint. It was found that this visually gives a very similar geometry and shows similar performance to using a maximum volume constraint.

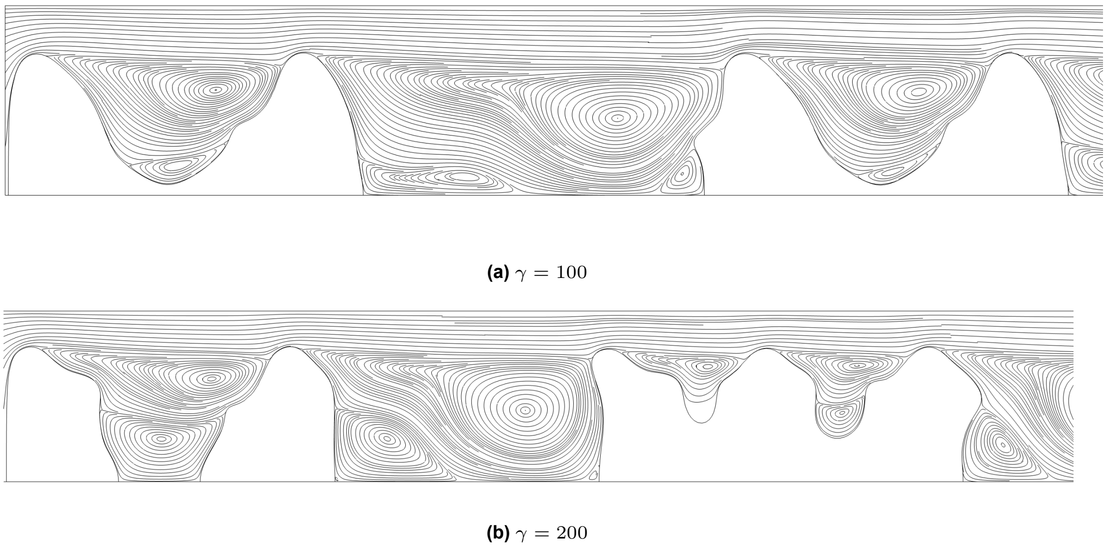

(a) $\gamma = 100$

(b) $\gamma = 200$

Figure 4.8: Streamlines in the first 0.007 meter of Ω_d for optimized designs with $Re = 200$ and different γ

4.3. Parametric description of the optimized structures

Manufacturing the exact topologically optimized designs is challenging. The geometry varies along the channel length, and the small local variations within each structure complicate fabrication. This motivates defining a single representative structure that is repeated across the channel and fully described by a small set of geometric parameters. Such a parametrization provides a clear and adjustable description of the geometry, enabling straightforward variation by adjusting the parameters. This section presents the procedure used to compute an average structure shape from all optimized designs, extract a corresponding parameter set, and compare the thermal performance of the parametrized structure to the original optimized design.

4.3.1. Defining the geometrical parameters

Because the structures exhibit similar rounded triangular shapes, each design is described using seven parameters. These parameters form the geometry shown in Figure 4.9. All parameters are defined in that figure except N, which denotes the number of structures placed along the channel; the remaining structures are arranged similarly to the two shown.

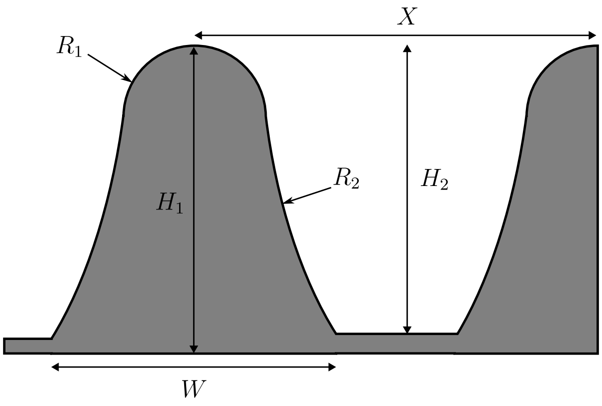

Figure 4.9: Parametric description of repeated structures

To determine these parameters for each optimized design, the geometries are processed using MATLAB (2024). First, the design is converted into an array of points representing the outer boundary of all structures. The individual structures are then identified and separated into smaller datasets, each corresponding to a single structure. The structures are normalized along the x-axis by subtracting the mean x-value of that dataset. These datasets are concatenated, and their mean is computed to obtain the average structure geometry.

The parameters are extracted from this mean geometry by taking the minima and maxima of the point cloud along the x- and y-axes and by fitting circles to the upper and side boundaries to determine the radii. An overview of the resulting parameters for all optimized designs is provided in Appendix A. Two examples comparing the calculated mean geometry with its parametrized counterpart are shown in Figure 4.10. While the shapes are not identical, they are closely aligned.

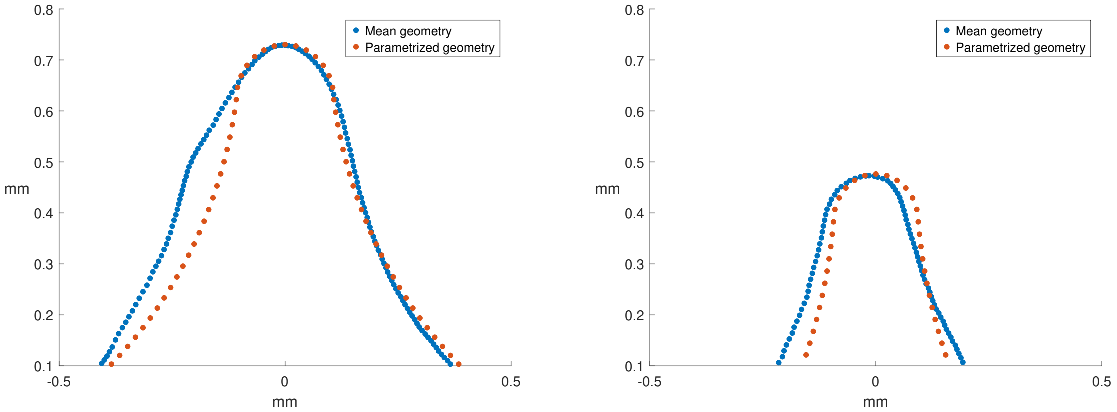

(a) $Re = 300$, $\gamma = 300$ **(b)** $Re = 100$, $\gamma = 10$

Figure 4.10: Shape comparison between average geometry and parametrized geometry for two designs

4.3.2. Performance comparison of parametrized structures

The parametrized designs are placed in a two-dimensional channel using the same input parameters as the optimized designs, listed in the right column of Table 4.1. The same triangular mesh is retained. The designs are compared in terms of pressure drop and HTC in Figure 4.11. Each dot represents a topologically optimized design, and each star represents the corresponding parametrized design. When the parametrized design performs similarly to the corresponding optimized design, the two data points should be close together in the plot.

Because some optimized designs did not yield well-defined geometric parameters, fewer parametrized designs are available for comparison at $Re = 100$ than optimized designs. Unfortunately, the designs lie quite far apart in the plots. For lower pressure drop, the data points are still quite close, but for high pressure drop, they are so far apart that it becomes unclear which designs belong together just looking at the plot.

As an illustration, the pressure fields of the optimized design and its parametrized counterpart corresponding to the geometry in Figure 4.9 are shown in Figure 4.12. The optimized design exhibits a significantly larger pressure drop. This difference is primarily due to two factors: the optimized design contains more peaks, and its upstream structure faces are more vertical. The discrepancy in the number of peaks arises because the parameter N in the parametrized geometry does not directly correspond to the number of peaks in the optimized design; designs dominated by a single large central structure naturally contain fewer peaks. In addition, the parametrized structures are symmetric, and their downstream faces are more curved, which forces their upstream faces to be less vertical than those in the optimized geometry.

4.3.3. Discussion on parametrized designs

Converting the optimized designs into parametrized structures resulted in large differences in pressure drop. Although all designs were processed using the same MATLAB script, their underlying topologies varied considerably, from tall, narrow peaks to broad central structures. Some showed strong variation in peak height, while others were nearly uniform. These geometric differences have a strong influence on pressure drop, and a single parametrization procedure cannot represent all cases equally well. This

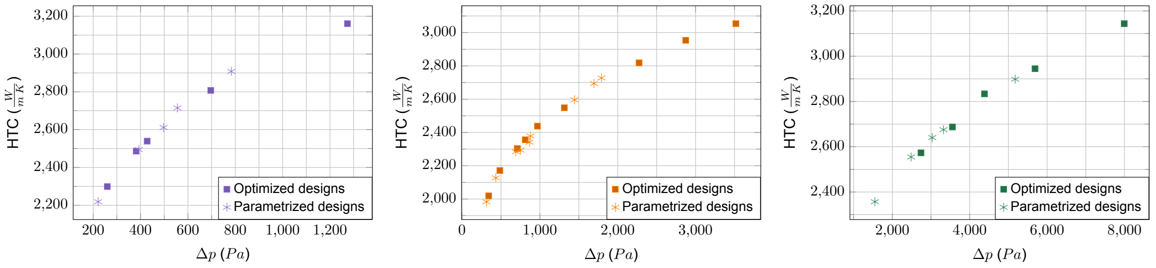

(a) $Re = 100$ **(b)** $Re = 200$ **(c)** $Re = 300$

Figure 4.11: Performance comparison for HTC against Δp for the optimized designs and corresponding parametrized designs

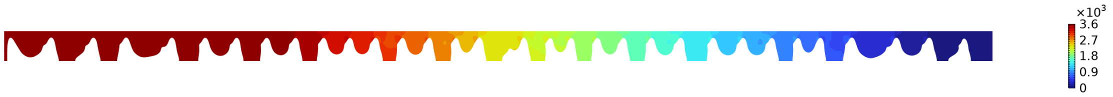

(a) Topologically optimized design. $\Delta p = 5688\ Pa$

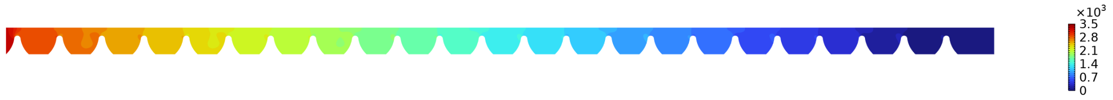

(b) Parametrized design. $\Delta p = 3322\ Pa$

Figure 4.12: Pressure field plotted over the Ω_d in Pascals for the design optimized with $Re = 300$ and $\gamma = 300$ and corresponding parametrized design

reflects a common issue in TO for flow and thermal problems: the optimized shapes are irregular, difficult to interpret, and not easily reduced to clean geometric features.

The parametrization step was intended to recover a more regularly repeated structure while showing the same performance as the optimized design. Despite the different flow behavior of the parametrized and optimized geometries, the key question is whether the parametrized structures achieve comparable performance. Performance is evaluated as HTC relative to the pressure drop. In Figure 4.11, better-performing designs lie closer to the upper-left corner. The results show that both the optimized and parametrized designs fall roughly along the same diagonal trend, with only minor deviations. This indicates that the parametrized designs achieve nearly the same performance as the optimized ones.

Conceptually, this is reasonable: each optimized design is obtained under a fixed pressure-drop constraint and is therefore tuned to perform well at that pressure drop. What is notable is that, despite substantial geometric and flow-field differences, the parametrized structures still reach similar performance levels. The next section demonstrates that this holds for all evaluated designs, which is the main reason a more refined parametrization strategy was not pursued further.

The following section presents a full performance comparison of all optimized designs and several reference geometries for multiple Reynolds numbers. This is used to assess whether each design performs best at the Reynolds number for which it was optimized, or whether other designs may outperform it under different flow conditions.

4.4. Performance results of all designs

To identify the best-performing designs for a given Reynolds number, all designs are evaluated at $Re = 100$, 200, and 300. Two reference geometries are included for comparison. The first is the reference design introduced in Section 3.2. The second consists of a single rectangular structure with length L_3. The geometries of both reference designs are shown in Figure 4.13, where H is varied to tune the pressure drop Δp. All designs are placed in the same channel with height $L_1 = 0.001\ m$. For each Reynolds number, three quantities are evaluated: HTC, T_{Γ_t}, and ω_{Ω_t}. The corresponding plots are shown in Figure 4.14, Figure 4.15, and Figure 4.16.

In the HTC plot Figure 4.14, nearly all designs fall on a single curve. The same is the case for the

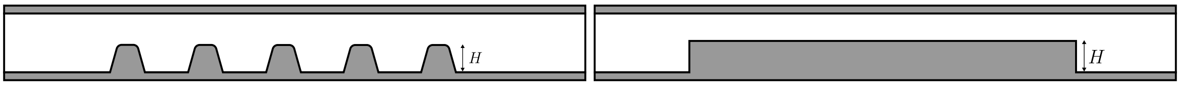

(a) Reference design 1 **(b)** Reference design 2

Figure 4.13: Two reference designs used to compare performance against optimized designs, where H can be varied to change the pressure drop

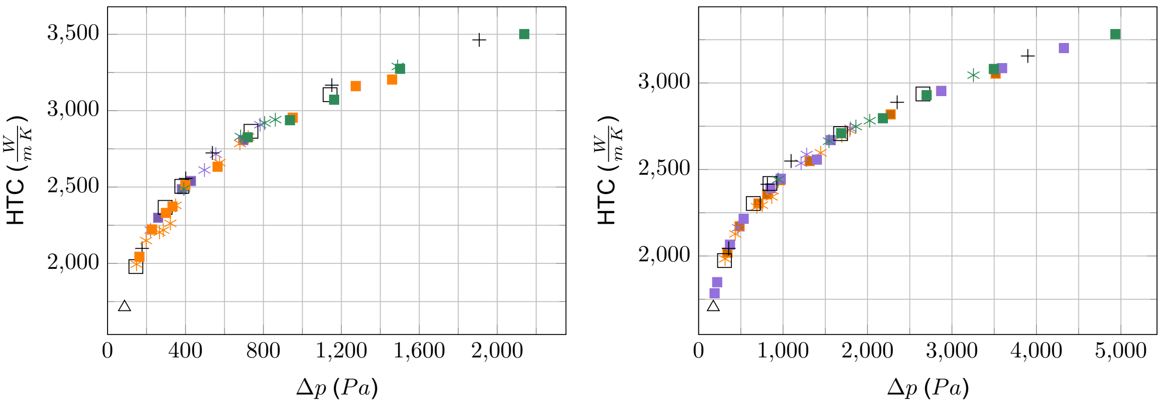

(a) $Re = 100$ **(b)** $Re = 200$

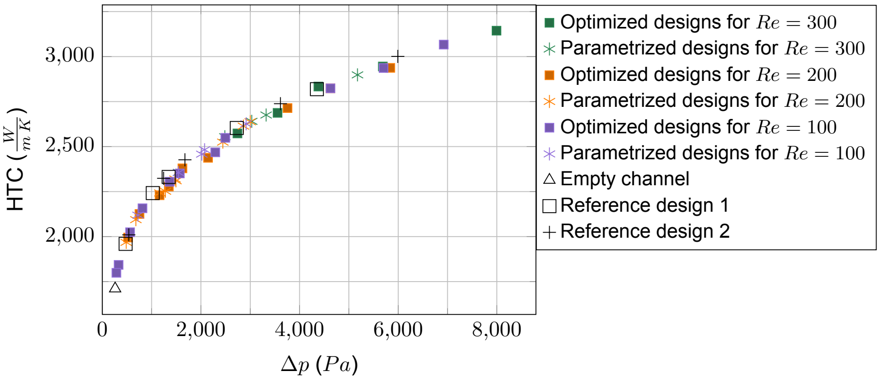

(c) $Re = 300$

Figure 4.14: Performance comparison for HTC against Δp for the optimized designs and corresponding parametrized designs

temperature plot Figure 4.15, which is as expected since all other parameters in the HTC calculation should be constant. The vorticity plots in Figure 4.16 show similar behavior. Unlike temperature-based metrics, the average vorticity increases nearly linearly with pressure drop, except at low pressure drop. At higher Δp, vorticity continues to increase while the temperature reduction becomes less pronounced. This agrees with observations reported by Lemenand et al. (2018).

4.5. Discussion on final results

The combined results from the previous analyses indicate that, under the conditions considered, the internal geometry of the channel does not significantly influence the overall thermal–hydraulic performance. Across all evaluated Reynolds numbers, a given pressure drop corresponds to a specific HTC, independent of the detailed structure layout. This indicated that the increase in HTC is mainly due to the increase in flow velocity near the boundary rather than due to the disruption of the fluid.

This raises the question of why the optimizer consistently converges to sharp-peaked structures instead of large rectangular ones. One explanation might be that the structures create somewhat higher vorticity in the near-wall region; however, Figure 4.16 indicates that the relation between vorticity and pressure drop is essentially identical across designs. More plausibly, all of these designs represent local minima under the imposed pressure-drop constraint, and the optimizer converges to one such configuration based on the path taken during optimization rather than physical performance differences.

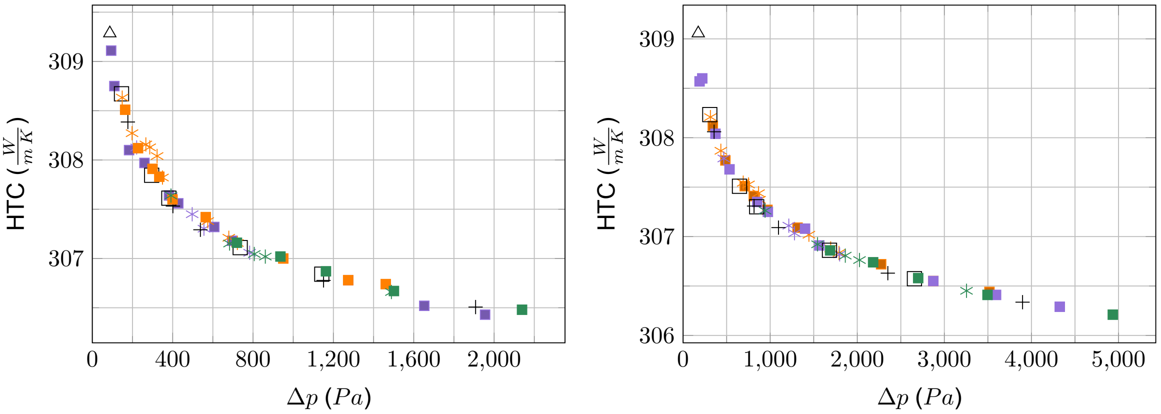

(a) $Re = 100$ **(b)** $Re = 200$

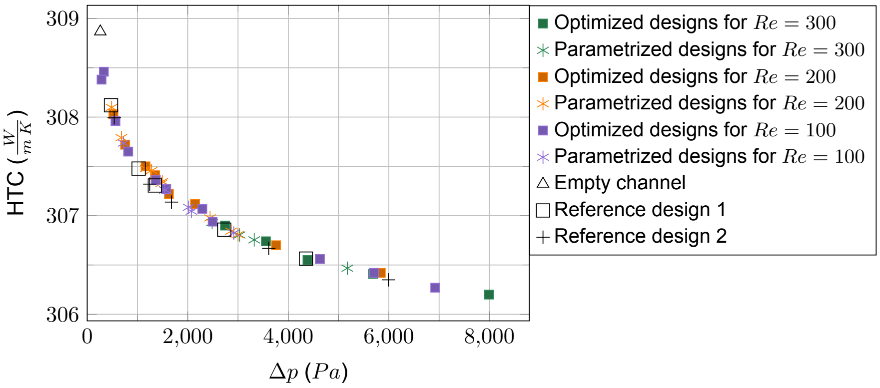

(c) $Re = 300$

Figure 4.15: PPerformance comparison of T_{Γ_t} against Δp for all designs analyzed at different Reynolds numbers

It is important to emphasize that the conclusion of geometry-independent performance applies only under the specific conditions of this study. Previous literature does report differences in thermal-hydraulic performance for different structure geometries. For example, Kumar (2019) show that semicircular grooves provide higher heat transfer, when corrected for pressure drop, compared to rectangular grooves. The main differences compared to the present study are that their structures are applied to both channel walls and that a turbulent flow model is used.

The formulation used in this thesis, in which structures are constrained to a single channel wall, strongly influences the optimization outcome. This restriction fixes the heated wall geometry and limits the available design freedom. Chapter 3 showed that attaching the structures to the heated wall can also show good performance. However, the recirculation zones can have a negative effect on the thermal performance since the heat can not be removed from this area. It is conceivable that designs with structures on both walls could exhibit higher performance and stronger geometry dependence. However, formulating such an optimization problem is more difficult. Using vorticity as an objective over the full domain results in designs such as Figure 3.5, while minimizing the length of the top boundary leads to large gray regions attached to the heated wall.

Within the laminar flow framework used throughout this study, the increase in heat transfer is dominated by the rise in flow velocity, implying that fluid mixing plays a limited role. Capturing heat-transfer enhancement due to flow disruption and mixing may therefore require a turbulent flow model, which can resolve additional vorticity and eddy-driven transport mechanisms. To explore this possibility, several optimized designs and the reference design two were evaluated using a turbulent SST model, as presented in Appendix D. In this exploratory analysis, differences in thermal–hydraulic performance between geometries were observed, indicating that performance can indeed become geometry dependent when turbulence effects are included. It should be stressed, however, that this turbulent study was limited in scope and intended primarily to guide future research.

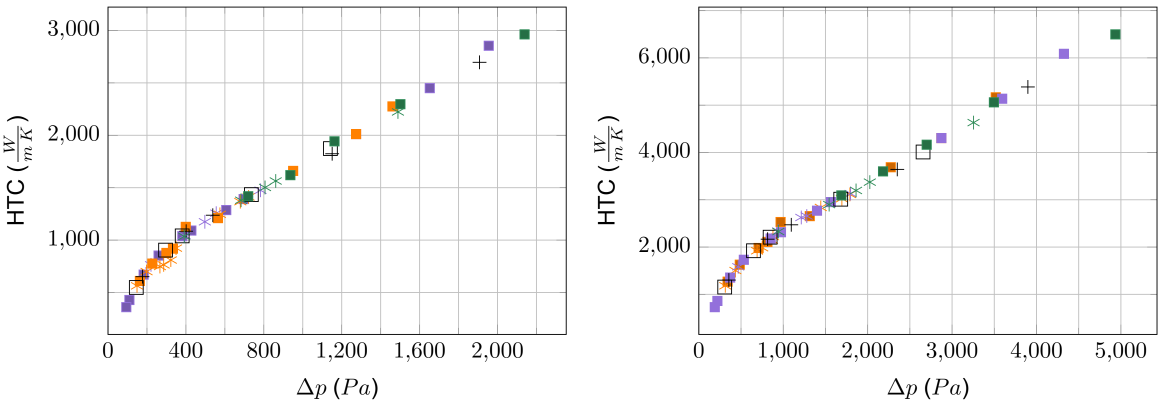

(a) $Re = 100$

(b) $Re = 200$

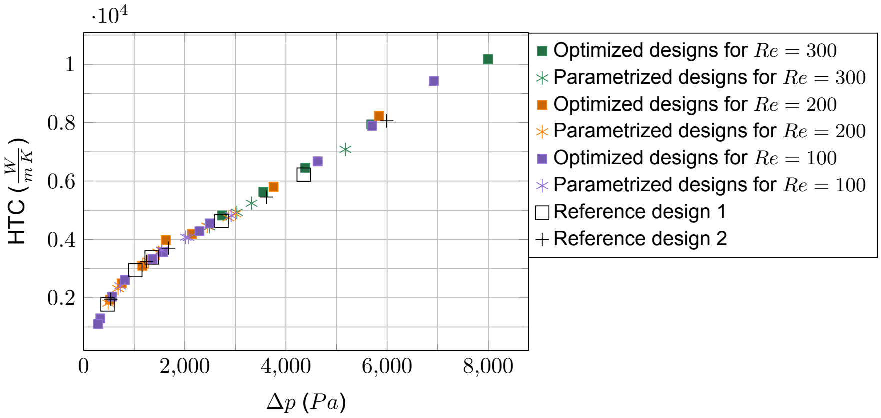

(c) $Re = 300$

Figure 4.16: Performance comparison of ω_{Ω_t} against Δp for all designs analyzed at different Reynolds numbers

5

Conclusions and recommendations

This thesis investigated the use of density-based TO to design wall-mounted structures that enhance heat transfer in a laminar flow cooling channel. The study addressed a set of sub-questions formulated in the introduction; their answers collectively support the final conclusion and inform recommendations for future master's theses or other research.

5.1. Sub-questions

All sub-questions are answered based on the research in this thesis:

- *What is an effective flow penalization method for accurately modeling the flow field and maintaining stability at relatively high laminar Reynolds numbers?*

Following Theulings et al. (2025), the Darcy-Forchheimer method was implemented. It yielded stable convergence and consistent results between porous and cutout designs for $Re = 100$ and 200. At $Re = 300$, convergence became less stable, and reliable results were only obtained for large pressure-drop constraints. For higher Re, the laminar solver showed significant stability issues and could no longer resolve the flow field accurately.

- *To what extent can vorticity be a substitute for a thermal objective when optimizing for heat transfer coefficient?*

Vorticity proved to be a suitable metric for maximizing HTC. Although there is no exact relationship, both the convergence history and final evaluations showed that HTC generally increases with vorticity. At high pressure drop, vorticity continues to grow while HTC increases more slowly, indicating an imperfect correlation. The choice to define vorticity only near the top boundary is effective for this problem, though maximizing vorticity throughout the full domain would be conceptually preferable.

- *How can solid structures be constrained to remain attached to the channel wall, considering manufacturability?*

Defining the vorticity objective near the heated wall successfully ensured that all structures remained attached to the opposite wall. If vorticity were defined across the full domain, a separate constraint formulation would be required to maintain manufacturable, wall-attached structures. This could potentially be done with a milling constraint; however, in this research, using this was unsuccessful.

- *Can different optimized designs be interpreted to identify trends and characteristics across various input conditions?*

Across varying Reynolds numbers and pressure drop constraints, several geometric trends were observed, such as rounded triangular features and increasing structural height with increasing pressure drop. However, the global thermal–hydraulic performance showed minimal dependence on geometry. For a given Δp, all designs produced nearly identical HTC, indicating that geometry plays a negligible role in overall performance under the studied conditions.

- *To what extent can the optimized designs be defined by a set of geometrical parameters and show similar performance?*

Optimized geometries were reduced to a parametric representation of repeated structures. Some of these parametrized designs, while capturing the average shape, produced flow fields and pressure drops that differed substantially from their corresponding optimized designs. Because global performance was ultimately geometry-independent, further refinement of the parametrization was not pursued.

5.2. Research question

Based on the answers to the subquestions, a final answer can be given to the research question, together with a conclusion to the thesis.

- *What are the optimal wall structures inside a flow channel under various flow conditions that maximize the heat transfer coefficient?*

The findings indicate that, within the scope of this study, there are no uniquely optimal wall structures. For a two-dimensional laminar channel heated on one wall, where structures are restricted to the opposite wall, all geometries in this study achieve approximately the same HTC when operating at the same pressure drop. Performance is therefore governed primarily by Δp, not by the specific structural shape. The performance gain is mainly due to the increase in flow velocity near the heated boundary, rather than to flow disruption and mixing.

5.3. Recommendations for future work

The conclusions of this thesis apply to a constrained, two-dimensional laminar channel with wall-mounted structures on a single boundary. To further understand how geometry, flow physics, and optimization formulation influence thermal–hydraulic performance, more research is recommended.

Optimize structures with turbulent model: In Appendix D, it was observed that performance differences can arise when a turbulent flow model is employed. Heat-transfer enhancement due to fluid mixing may therefore only become apparent when turbulence is explicitly modeled. Conducting a study similar to the present one, but based on a turbulent flow formulation, could reveal genuinely optimal structure geometries. However, combining density-based topology optimization with turbulence modeling is likely to introduce significant numerical and modeling challenges. As a result, alternative optimization approaches, such as level-set topology optimization or shape optimization, in which boundaries are clearly defined, may be more suitable for such investigations.

TO for high Reynolds numbers: Achieving stable convergence for $Re \geq 300$ remains a challenge. Incorporating the penalization term directly into the SUPG formulation, as proposed by Alexandersen, Aage, et al. (2014), may improve robustness but requires numerical modifications that were difficult to implement in COMSOL (see Appendix B). A different solution is to use turbulence models, since localized turbulence may arise in regions with large velocity gradients even when the inlet Reynolds number is nominally laminar.

Structures on both channel walls: This thesis only considered structures on one wall at a time. Allowing structures on both walls could increase mixing and surface area without necessarily creating detrimental recirculation zones.

Multiple heated walls: Applying heat flux to both channel walls would fundamentally change the thermal performance of the designs. The recirculation zones between the structures may become detrimental by trapping thermal energy. Optimized geometries for this condition may require structures on both walls or alternative flow-conditioning features.

Three-dimensional optimization: Extending the optimization to three dimensions would capture secondary flows and spanwise mixing that are impossible to represent in 2D. Vorticity would have three components instead of only the out-of-plane component. A promising metric to maximize is Helicity, which is a metric for the amount of vorticity in the flow direction of the fluid. Constraints would be required to avoid non-manufacturable shapes, such as isolated bodies or deeply undercut features. Due to the significantly higher computational cost, a robust and well-validated optimization and stabilization strategy should be established beforehand.

Alternative flow-disrupting techniques: Beyond wall-mounted structures, other mechanisms such as curved channels, periodic bends, or sudden expansions can generate vortical structures (e.g., Dean vortices) that enhance mixing. Investigating these geometries within a consistent optimization framework may identify more effective methods of boosting HTC for a given pressure drop.

Reduced-order models incorporating 3D effects: Performing an optimization on a fully three-dimensional flow model is costly. Therefore, it would be beneficial to be able to use a two- or even one-dimensional model with some kind of added thermal effect due to three-dimensional flow effects. As an example, defining a cooling plate with one-dimensional channels. When these channels make a bend, the thermal performance goes up due to the Dean vortices, but the pressure drop also increases.

References

Alexandersen, Joe (Jan. 2023). “A detailed introduction to density-based topology optimisation of fluid flow problems with implementation in MATLAB”. In: *Structural and Multidisciplinary Optimization* 66 (1), pp. 1–38. ISSN: 16151488. DOI: `10.1007/S00158-022-03420-9/FIGURES/28`. URL: `https://link.springer.com/article/10.1007/s00158-022-03420-9`.

Alexandersen, Joe, Niels Aage, et al. (Dec. 2014). “Topology optimisation for natural convection problems”. In: *International Journal for Numerical Methods in Fluids* 76 (10), pp. 699–721. ISSN: 10970363. DOI: `10.1002/fld.3954`.

Alexandersen, Joe and Casper Schousboe Andreasen (Mar. 2020). “A Review of Topology Optimisation for Fluid-Based Problems”. In: *Fluids 2020, Vol. 5, Page 29* 5 (1), p. 29. ISSN: 2311-5521. DOI: `10.3390/FLUIDS5010029`. URL: `https://www.mdpi.com/2311-5521/5/1/29/htm%20https://www.mdpi.com/2311-5521/5/1/29`.

Arvanitis, Konstantinos D., Demetri Bouris, and Elias Papanicolaou (Aug. 2018). “Laminar flow and heat transfer in U-bends: The effect of secondary flows in ducts with partial and full curvature”. In: *International Journal of Thermal Sciences* 130, pp. 70–93. ISSN: 1290-0729. DOI: `10.1016/J.IJTHERMALSCI.2018.03.027`. URL: `https://www.sciencedirect.com/science/article/pii/S1290072917307986`.

Borrvall, Thomas and Joakim Petersson (Jan. 2003). “Topology optimization of fluids in Stokes flow”. In: *International Journal for Numerical Methods in Fluids* 41 (1), pp. 77–107. ISSN: 02712091. DOI: `10.1002/fld.426`.

Dbouk, T. (Feb. 2017). “A review about the engineering design of optimal heat transfer systems using topology optimization”. In: *Applied Thermal Engineering* 112, pp. 841–854. ISSN: 1359-4311. DOI: `10.1016/J.APPLTHERMALENG.2016.10.134`.

Dede, Ercan (2009). *Multiphysics Topology Optimization of Heat Transfer and Fluid Flow Systems*. Tech. rep. Toyota Research Institute of North America. URL: `https://www.comsol.com/paper/multiphysics-topology-optimization-of-heat-transfer-and-fluid-flow-systems-6282`.

Dilgen, Sumer B. et al. (May 2018). “Density based topology optimization of turbulent flow heat transfer systems”. In: *Structural and Multidisciplinary Optimization* 57 (5), pp. 1905–1918. ISSN: 16151488. DOI: `10.1007/S00158-018-1967-6/FIGURES/13`. URL: `https://link.springer.com/article/10.1007/s00158-018-1967-6`.

Gersborg-Hansen, A., O. Sigmund, and R. B. Haber (Sept. 2005). “Topology optimization of channel flow problems”. In: *Structural and Multidisciplinary Optimization* 30 (3), pp. 181–192. ISSN: 1615147X. DOI: `10.1007/s00158-004-0508-7`.

Høghøj, Lukas C. and Erik A. Träff (Mar. 2022). “An advection–diffusion based filter for machinable designs in topology optimization”. In: *Computer Methods in Applied Mechanics and Engineering* 391, p. 114488. ISSN: 0045-7825. DOI: `10.1016/J.CMA.2021.114488`. URL: `https://www.sciencedirect.com/science/article/pii/S0045782521007003`.

Kumar, Pankaj (Feb. 2019). “Numerical investigation of fluid flow and heat transfer in trapezoidal microchannel with groove structure”. In: *International Journal of Thermal Sciences* 136, pp. 33–43. ISSN: 1290-0729. DOI: `10.1016/J.IJTHERMALSCI.2018.10.006`. URL: `https://www.sciencedirect.com/science/article/pii/S1290072918300474#fig2`.

Lazarov, B. S. and O. Sigmund (Dec. 2010). “Filters in topology optimization based on Helmholtz-type differential equations”. In: *International Journal for Numerical Methods in Engineering* 86 (6), pp. 765–781. ISSN: 00295981. DOI: `10.1002/NME.3072;WGROUP:STRING:PUBLICATION`. URL: `/doi/pdf/10.1002/nme.3072%20https://onlinelibrary.wiley.com/doi/abs/10.1002/nme.3072%20https://onlinelibrary.wiley.com/doi/10.1002/nme.3072`.

Lemenand, Thierry et al. (Mar. 2018). “Vorticity and convective heat transfer downstream of a vortex generator”. In: *International Journal of Thermal Sciences* 125, pp. 342–349. ISSN: 1290-0729. DOI: `10.1016/J.IJTHERMALSCI.2017.11.021`. URL: `https://www.sciencedirect.com/science/article/pii/S129007291630059X?fr=RR-2&ref=pdf_download&rr=995929cd0b9fa6a3`.

Li, Xinlei et al. (Jan. 2025). “Topology optimization of regenerative cooling structures under high Reynolds number flow with variable thermo-physical properties”. In: *Applied Thermal Engineering* 258, p. 124602. ISSN: 1359-4311. DOI: 10.1016/J.APPLTHERMALENG.2024.124602. URL: https://www.sciencedirect.com/science/article/pii/S1359431124022701?casa_token=QL088WdT6K0AAAAA:leCnKxAijPah7Ejiq5qnXh1EYA7QYtgYNZyFMbDCQxhfQTO_nRu75Nii3aalS-ht05UAHtpiVw.

MATLAB (2024). *MATLAB version: 24.2.0 (R2024b)*. Natick, Massachusetts, United States. URL: https://www.mathworks.com.

Menter, F. R. (Aug. 1994). “Two-equation eddy-viscosity turbulence models for engineering applications”. In: *AIAA Journal* 32 (8), pp. 1598–1605. ISSN: 0001-1452. DOI: 10.2514/3.12149.

Mori, Yasuo and Wataru Nakayama (May 1967). “Study on forced convective heat transfer in curved pipes: (3rd report, theoretical analysis under the condition of uniform wall temperature and practical formulae)”. In: *International Journal of Heat and Mass Transfer* 10 (5), pp. 681–695. ISSN: 0017-9310. DOI: 10.1016/0017-9310(67)90113-5. URL: https://www.sciencedirect.com/science/article/pii/0017931067901135.

Multiphysics®, COMSOL (2023). *COMSOL Multiphysics® v. 6.2.* Stockholm, Sweden. URL: www.comsol.com.

Philippi, B. and Y. Jin (Dec. 2015). “Topology Optimization of Turbulent Fluid Flow with a Sensitive Porosity Adjoint Method (SPAM)”. In: URL: https://arxiv.org/pdf/1512.08445.

Ramadhan, Abdulmajeed A., Yaser T. Al Anii, and Amer J. Shareef (Feb. 2013). “Groove geometry effects on turbulent heat transfer and fluid flow”. In: *Heat and Mass Transfer/Waerme- und Stoffuebertragung* 49 (2), pp. 185–195. ISSN: 09477411. DOI: 10.1007/S00231-012-1076-9/FIGURES/13. URL: https://link.springer.com/article/10.1007/s00231-012-1076-9.

Rogié, Brice and Casper Schousboe Andreasen (Jan. 2023). “Design complexity tradeoffs in topology optimization of forced convection laminar flow heat sinks”. In: *Structural and Multidisciplinary Optimization* 66 (1), pp. 1–22. ISSN: 16151488. DOI: 10.1007/S00158-022-03449-W/FIGURES/24. URL: https://link.springer.com/article/10.1007/s00158-022-03449-w.

Sanhueza, Rafael Diez and Jurriaan W.R. Peeters (Nov. 2025). “Data-driven optimization of rough surfaces for convective heat transfer enhancement”. In: *International Journal of Heat and Mass Transfer* 251, p. 127313. ISSN: 0017-9310. DOI: 10.1016/J.IJHEATMASSTRANSFER.2025.127313. URL: https://www.sciencedirect.com/science/article/pii/S0017931025006520.

Subramaniam, V., T. Dbouk, and J. L. Harion (Feb. 2019). “Topology optimization of conjugate heat transfer systems: A competition between heat transfer enhancement and pressure drop reduction”. In: *International Journal of Heat and Fluid Flow* 75, pp. 165–184. ISSN: 0142727X. DOI: 10.1016/j.ijheatfluidflow.2019.01.002.

Svanberg, Krister (2007). “MMA and GCMMA – two methods for nonlinear optimization”. In: *Report, KTH*. URL: https://people.kth.se/~krille/mmagcmma.pdf.

Tezduyar, Tayfun and Sunil Sathe (June 2002). *Stabilization Parameters in SUPG and PSPG Formulations*. Tech. rep. Journal of Computational and Applied Mechanics.

Theulings, M. J.B. et al. (Aug. 2025). “Reducing parameter tuning in topology optimization of flow problems using a Darcy and Forchheimer penalization”. In: *Computer Methods in Applied Mechanics and Engineering* 443, p. 118027. ISSN: 0045-7825. DOI: 10.1016/J.CMA.2025.118027. URL: https://www.sciencedirect.com/science/article/pii/S0045782525002993?dgcid=rss_sd_all.

Wang, Fengwen, Boyan Stefanov Lazarov, and Ole Sigmund (Dec. 2010). “On projection methods, convergence and robust formulations in topology optimization”. In: *Structural and Multidisciplinary Optimization 2010 43:6* 43 (6), pp. 767–784. ISSN: 1615-1488. DOI: 10.1007/S00158-010-0602-Y. URL: https://link.springer.com/article/10.1007/s00158-010-0602-y.

Zhao, Xi et al. (2018). “A “poor man’s approach” to topology optimization of cooling channels based on a Darcy flow model”. In: *International Journal of Heat and Mass Transfer* 116, pp. 1108–1123. ISSN: 00179310. DOI: 10.1016/j.ijheatmasstransfer.2017.09.090. URL: https://doi.org/10.1016/j.ijheatmasstransfer.2017.09.090.

A

Overview designs

The values of all geometrical parameters for the parametrized designs

Re	γ	**H1**	**H2**	**R1**	**R2**	**W1**	**X1**	**X2**	**N**
100	10	0.4764	0.4764	0.0938	1.0353	0.4077	2.7778	1.1994	12
100	20	0.6435	0.631	0.0974	1.1831	0.6937	2.0833	2.2239	16
100	25	0.6835	0.6553	0.11	1.1798	0.6866	1.2821	2.1989	26
100	50	0.6728	0.5932	0.1089	0.8252	0.7946	1.2346	1.5242	27
100	100	0.7121	0.489	0.1278	0.5931	0.7242	1.0101	1.2744	33
200	5	0.3761	0.294	0.275	0	0.8317	1.9608	1.6492	17
200	10	0.4733	0.4227	0.1032	0.889	0.5652	1.3333	1.7741	25
200	20	0.6155	0.6155	0.116	1.132	0.7263	1.9608	3.4983	17
200	25	0.6444	0.6444	0.1222	1.2977	0.8242	1.9608	3.5482	17
200	40	0.6685	0.6164	0.1297	0.732	0.9629	1.6667	3.6232	20
200	50	0.6508	0.5297	0.1289	0.6829	0.9344	1.5873	2.7236	21
200	100	0.7147	0.6165	0.1686	0.6997	0.9568	1.4493	2.3238	23
200	150	0.7259	0.5574	0.2001	0	0.9392	1.3333	2.1239	25
200	200	0.7264	0.4182	0.1582	0	0.7866	1.1905	1.8741	28
300	300	0.7373	0.5189	0.1102	0.429	0.98	1.0101	0.8996	33
300	100	0.6425	0.565	0.09	0.6025	1.0175	1.5873	2.2489	21
300	150	0.6915	0.5815	0.0909	0.5603	0.9601	1.2346	1.2244	27
300	200	0.717	0.6366	0.1057	0.7317	0.845	1.1494	1.3243	29
300	300	0.7301	0.6266	0.1079	0.8778	0.7683	1.0417	1.4243	32
300	600	0.7583	0.6179	0.1015	0.8703	0.6934	0.8772	0.6747	38

All parameters in mm

The final design fields for all optimized designs

Re=100

$\gamma = 200$

$\gamma = 150$

$\gamma = 100$

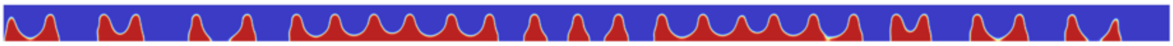

$\gamma = 50$

$\gamma = 40$

$\gamma = 25$

$\gamma = 20$

$\gamma = 10$

$\gamma = 5$

$\gamma = 2$

$\gamma = 1.5$

Re=200

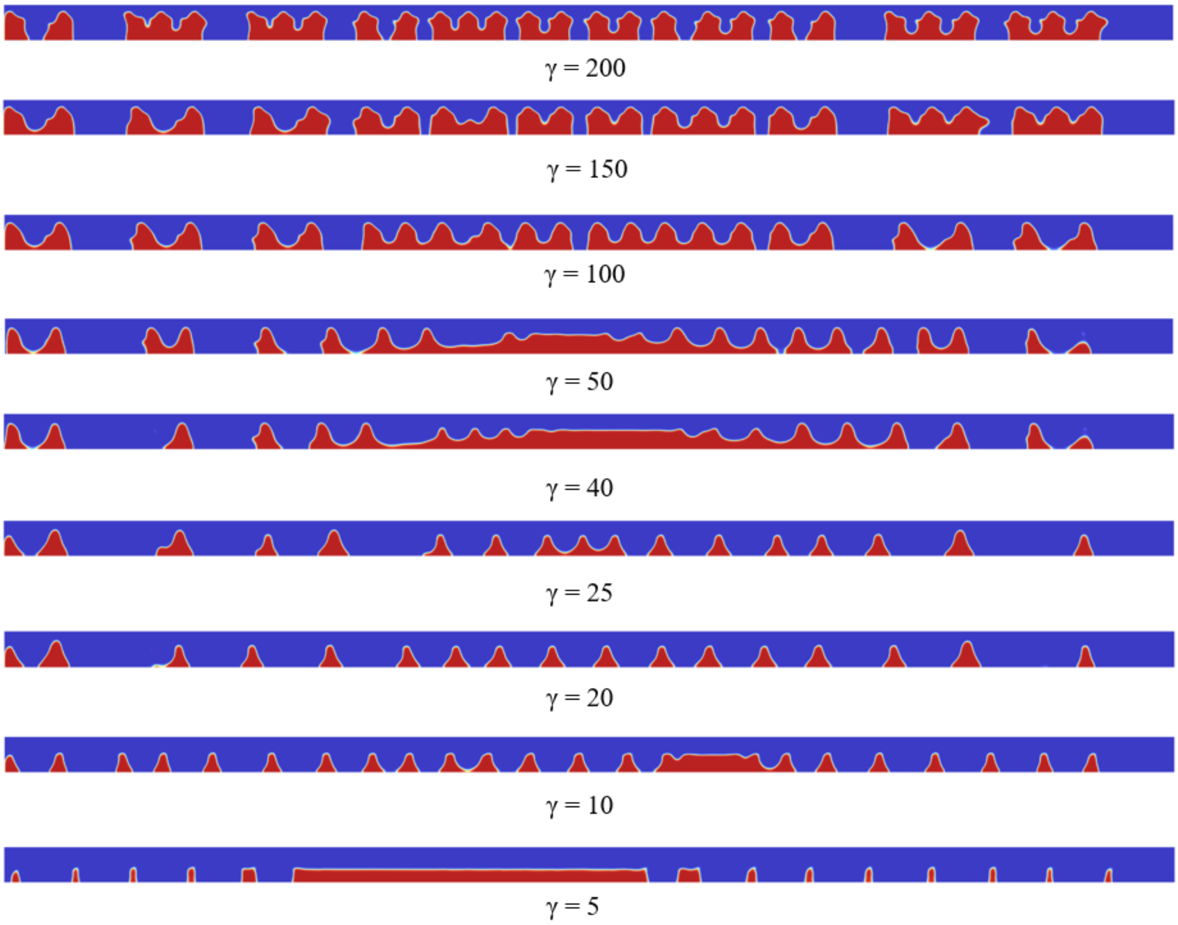

Re=300

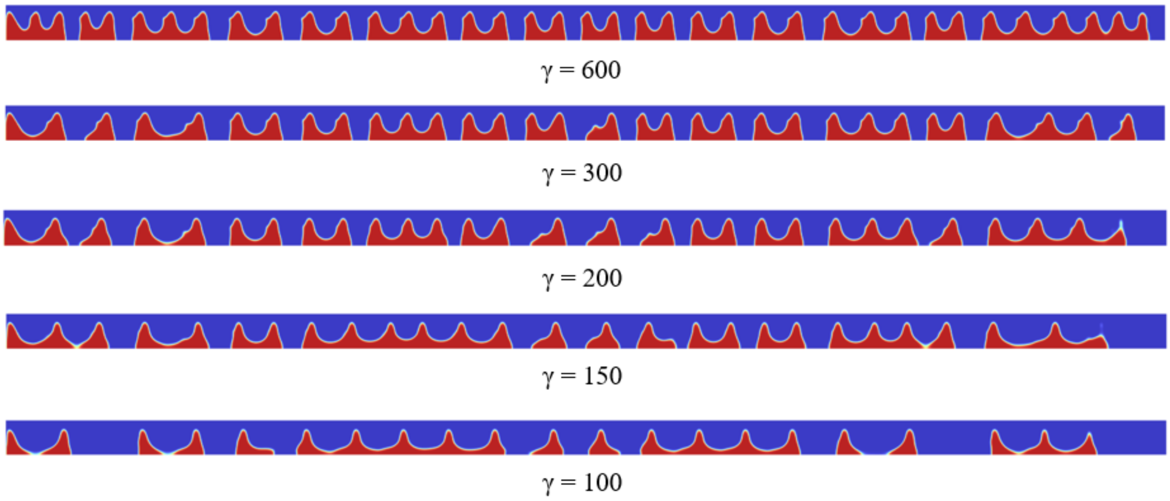

B

Manual flow stabilization in COMSOL

To improve the stability of the topology optimization at higher Reynolds numbers, an additional Darcy–Forchheimer term can be incorporated into the flow stabilization. Alexandersen, Aage, et al. (2014) used SUPG and PSPG stabilization with an added Darcy penalization term in the definition of the stabilization parameter. In this thesis, an attempt was made to implement a similar approach for Darcy–Forchheimer penalization in COMSOL Multiphysics.

The first step is to add the SUPG and PSPG terms to the weak formulation of the Navier–Stokes equations. These terms take the form:

$$\text{SUPG: } \int_\Omega \tau_{SU}\, u_j \frac{\partial w_i}{\partial x_j} R_i \, dV, \tag{B.1}$$

$$\text{PSPG: } \int_\Omega \frac{\tau_{PS}}{\rho} \frac{\partial q}{\partial x_i} R_i \, dV, \tag{B.2}$$

where w_i is the test function associated with the velocity component u_i, q is the test function associated with the pressure p, ρ is the fluid density, and R_i is the residual of the momentum equation. The stabilization parameters, including the Darcy–Forchheimer contribution, are defined as:

$$\tau_{SU} = \left(\frac{1}{\tau_1} + \frac{1}{\tau_3} + \left(D(\alpha) + F(\alpha) \, \|\mathbf{u}\| \right) \right)^{-\frac{1}{2}}, \tag{B.3}$$

$$\tau_{PS} = \tau_{SU}, \tag{B.4}$$

where

$$\tau_1 = \frac{h_{UGN}}{\|\mathbf{u}\|}, \tag{B.5}$$

$$\tau_3 = \frac{h_{RGN}^2}{4Pr}, \tag{B.6}$$

$$h_{UGN} = 2\|\mathbf{u}\| \left(\sum_{a=1}^{n_{en}} |\mathbf{u} \cdot \nabla N_{ua}| \right)^{-1} \tag{B.7}$$

$$h_{RGN} = 2 \left(\sum_{a=1}^{n_{en}} |\mathbf{r} \cdot \nabla N_{ua}| \right)^{-1}, \tag{B.8}$$

$$\mathbf{r} = \frac{\nabla\|\mathbf{u}\|}{\|\nabla\|\mathbf{u}\|\|}, \tag{B.9}$$

n_{en} is the number of nodes per element, N_{ua} is the velocity shape function for node a, and Pr is the Prandtl number. The length scales h_{UGN} and h_{RGN} are defined as in Tezduyar and Sathe (2002).

Since COMSOL Multiphysics does not allow modification of its built-in streamline diffusion stabilization, the SUPG and PSPG terms were manually added as an extra weak contribution. Initially, this was attempted without the Darcy–Forchheimer term. The procedure followed is outlined below.

First, a new two-dimensional model with laminar flow physics using P2+P1 elements was created. Under ”Laminar Flow”, a “Weak Contribution” node was added and applied to all flow domains. Separate weak-form nodes were used for the SUPG and PSPG terms. The required weak expressions were implemented using COMSOL syntax:

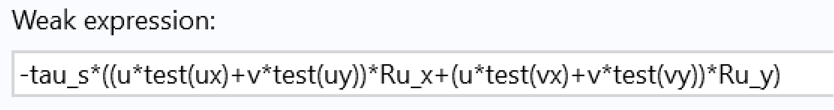

Weak expression:

```
-tau_s*((u*test(ux)+v*test(uy))*Ru_x+(u*test(vx)+v*test(vy))*Ru_y)
```

(a) SUPG

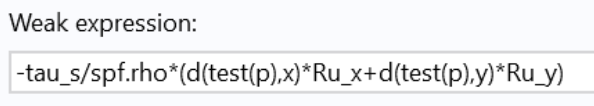

Weak expression:

```
-tau_s/spf.rho*(d(test(p),x)*Ru_x+d(test(p),y)*Ru_y)
```

(b) PSPG

All parameters that are not automatically defined in COMSOL are defined under a variable node as follows:

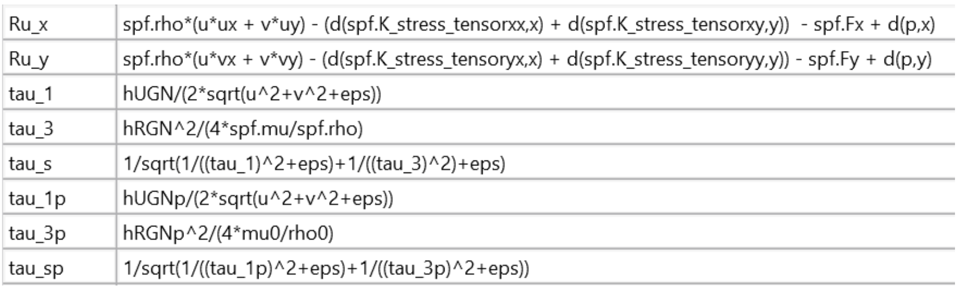

Ru_x	spf.rho*(u*ux + v*uy) - (d(spf.K_stress_tensorxx,x) + d(spf.K_stress_tensorxy,y)) - spf.Fx + d(p,x)
Ru_y	spf.rho*(u*vx + v*vy) - (d(spf.K_stress_tensoryx,x) + d(spf.K_stress_tensoryy,y)) - spf.Fy + d(p,y)
tau_1	hUGN/(2*sqrt(u^2+v^2+eps))
tau_3	hRGN^2/(4*spf.mu/spf.rho)
tau_s	1/sqrt(1/((tau_1)^2+eps)+1/((tau_3)^2)+eps)
tau_1p	hUGNp/(2*sqrt(u^2+v^2+eps))
tau_3p	hRGNp^2/(4*mu0/rho0)
tau_sp	1/sqrt(1/((tau_1p)^2+eps)+1/((tau_3p)^2+eps))

The UGN and RGN length scales require the velocity and pressure shape functions. However, COMSOL does not provide direct access to these shape functions, so they must be defined manually using the local coordinates ξ_1 and ξ_2. Since the pressure uses linear interpolation and the velocity uses quadratic interpolation, both types of shape functions were defined:

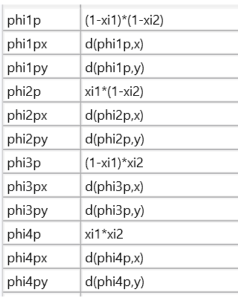

phi1p	(1-xi1)*(1-xi2)
phi1px	d(phi1p,x)
phi1py	d(phi1p,y)
phi2p	xi1*(1-xi2)
phi2px	d(phi2p,x)
phi2py	d(phi2p,y)
phi3p	(1-xi1)*xi2
phi3px	d(phi3p,x)
phi3py	d(phi3p,y)
phi4p	xi1*xi2
phi4px	d(phi4p,x)
phi4py	d(phi4p,y)

(a) Linear

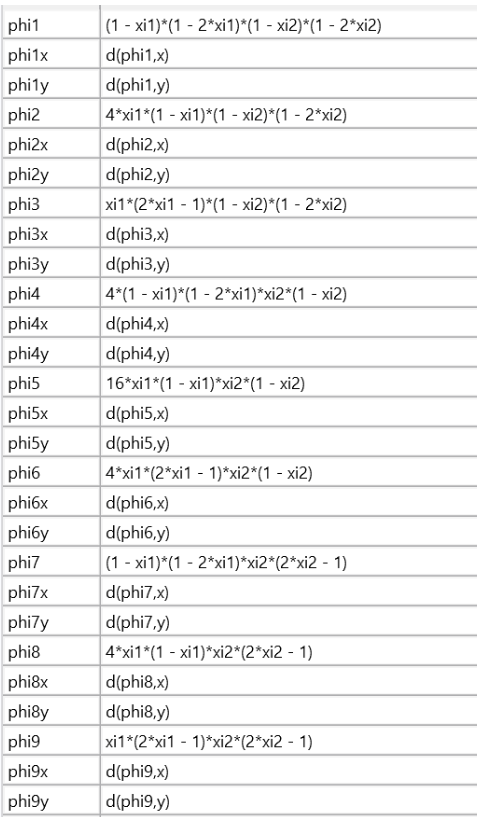

phi1	(1 - xi1)*(1 - 2*xi1)*(1 - xi2)*(1 - 2*xi2)
phi1x	d(phi1,x)
phi1y	d(phi1,y)
phi2	4*xi1*(1 - xi1)*(1 - xi2)*(1 - 2*xi2)
phi2x	d(phi2,x)
phi2y	d(phi2,y)
phi3	xi1*(2*xi1 - 1)*(1 - xi2)*(1 - 2*xi2)
phi3x	d(phi3,x)
phi3y	d(phi3,y)
phi4	4*(1 - xi1)*(1 - 2*xi1)*xi2*(1 - xi2)
phi4x	d(phi4,x)
phi4y	d(phi4,y)
phi5	16*xi1*(1 - xi1)*xi2*(1 - xi2)
phi5x	d(phi5,x)
phi5y	d(phi5,y)
phi6	4*xi1*(2*xi1 - 1)*xi2*(1 - xi2)
phi6x	d(phi6,x)
phi6y	d(phi6,y)
phi7	(1 - xi1)*(1 - 2*xi1)*xi2*(2*xi2 - 1)
phi7x	d(phi7,x)
phi7y	d(phi7,y)
phi8	4*xi1*(1 - xi1)*xi2*(2*xi2 - 1)
phi8x	d(phi8,x)
phi8y	d(phi8,y)
phi9	xi1*(2*xi1 - 1)*xi2*(2*xi2 - 1)
phi9x	d(phi9,x)
phi9y	d(phi9,y)

(b) Quadratic

The length scales are then defined as follows:

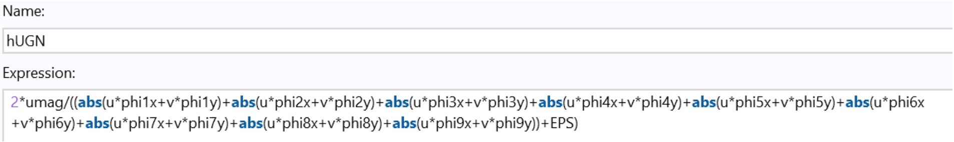

Name:

hUGN

Expression:

2*umag/((abs(u*phi1x+v*phi1y)+abs(u*phi2x+v*phi2y)+abs(u*phi3x+v*phi3y)+abs(u*phi4x+v*phi4y)+abs(u*phi5x+v*phi5y)+abs(u*phi6x
+v*phi6y)+abs(u*phi7x+v*phi7y)+abs(u*phi8x+v*phi8y)+abs(u*phi9x+v*phi9y))+EPS)

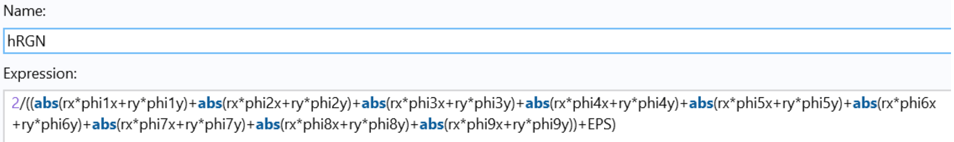

Name:

hRGN

Expression:

2/((abs(rx*phi1x+ry*phi1y)+abs(rx*phi2x+ry*phi2y)+abs(rx*phi3x+ry*phi3y)+abs(rx*phi4x+ry*phi4y)+abs(rx*phi5x+ry*phi5y)+abs(rx*phi6x
+ry*phi6y)+abs(rx*phi7x+ry*phi7y)+abs(rx*phi8x+ry*phi8y)+abs(rx*phi9x+ry*phi9y))+EPS)

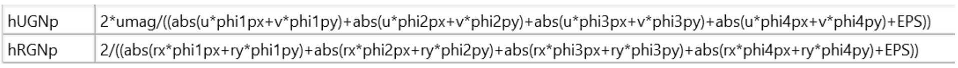

hUGNp	2*umag/((abs(u*phi1px+v*phi1py)+abs(u*phi2px+v*phi2py)+abs(u*phi3px+v*phi3py)+abs(u*phi4px+v*phi4py)+EPS))
hRGNp	2/((abs(rx*phi1px+ry*phi1py)+abs(rx*phi2px+ry*phi2py)+abs(rx*phi3px+ry*phi3py)+abs(rx*phi4px+ry*phi4py)+EPS))

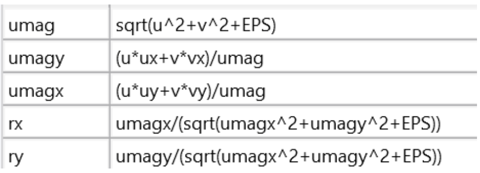

umag	sqrt(u^2+v^2+EPS)
umagy	(u*ux+v*vx)/umag
umagx	(u*uy+v*vy)/umag
rx	umagx/(sqrt(umagx^2+umagy^2+EPS))
ry	umagy/(sqrt(umagx^2+umagy^2+EPS))

Test model

To test the stabilization, a simple two-dimensional channel geometry (4 × 1) containing a solid square of side 0.5 was used. The domain was discretized with square elements of size 0.05. A fully developed inlet velocity was applied, dependent on the Reynolds number, and a zero-pressure condition was set at the outlet. Without stabilization, this model can be solved, but oscillations appear in the velocity field near the solid, as shown in Figure B.4.

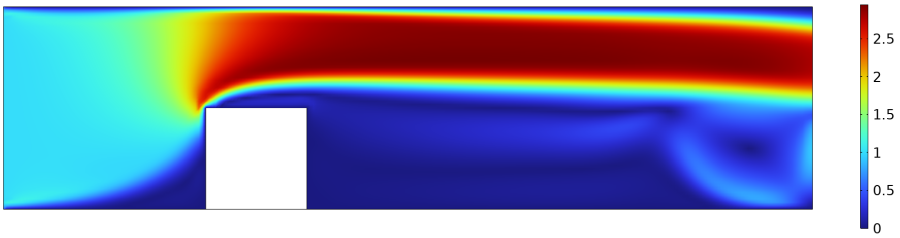

(a) With built-in streamline diffusion turned on

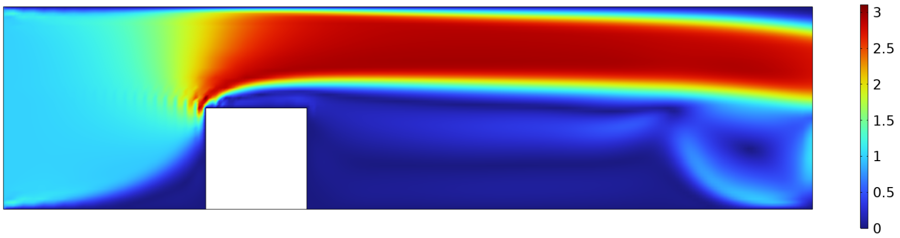

(b) Without any flow stabilization

Figure B.4: Velocity magnitude plotted over the domain for test model in m/s with $Re = 900$

Resulting problems

Adding the manually implemented stabilization led to unexpected behavior. The flow solver converged only for very low Reynolds numbers, and even then the velocity field differed from the solution obtained using COMSOL's built-in streamline diffusion. At higher Reynolds numbers, the solver failed to converge entirely, and the convergence behavior changed between runs, even when recomputing without altering any settings.

Because it was unclear whether the manually defined length scales were correctly implemented, a simplified approach was tested in which the length scales were set equal to the mesh size, 0.005. This worked for the test model, allowing convergence and producing a correct velocity field. However, when used together with the Darcy–Forchheimer term during topology optimization, the method again became unstable. This suggests that the correct formulation of the UGN and RGN length scales is essential for achieving stable behavior.

C

Minimum volume constraint

Since the volume constraint was never active in all optimizations, a test was done on using a minimum volume constraint. This results in a visually very similar design, with the rounded triangular features and a larger structure in the middle. The values of the different performance parameters are also very similar, indicating that using a minimum or maximum volume constraint does not have a big influence.

Figure C.1: α plotted over design domain optimized with minimum volume constraint of $V_f = 0.1$ with $Re = 200$ and $\gamma = 20$ and maximizing average vorticity magnitude over Ω_t

	V	Cutoff value	$\Delta p\ (Pa)$	HTC ($\frac{W}{m\,K}$)	$T_{\Gamma_t}\ (K)$	$\omega_{\Omega_t}\ (\frac{1}{s})$
min	0.4174	0.1	1145	2486	307.19	2453
max	0.2689	0.11	1120	2453	307.22	2446

Table C.1: Performance of cutout designs optimized with maximum volume constraint of $V_f = 0.4$ or minimum volume constraint with $V_f = 0.1$ with $Re = 300$ and $\gamma = 300$

D

Performance comparison with turbulence model

To assess whether performance gains due to flow mixing can be captured using a turbulence model, several optimized designs and the second reference design, evaluated at multiple structure heights, are analyzed using an SST turbulence model. As shown in Figure D.1, the reference designs continue to follow the same pressure-drop–HTC relationship observed previously. In contrast, the optimized designs exhibit significantly higher HTC values for the same pressure drop. This indicates that, when turbulence-induced mixing is resolved, the simple pressure-drop–HTC relationship no longer holds. Further research is required to confirm this behavior and to identify the corresponding optimal geometries.

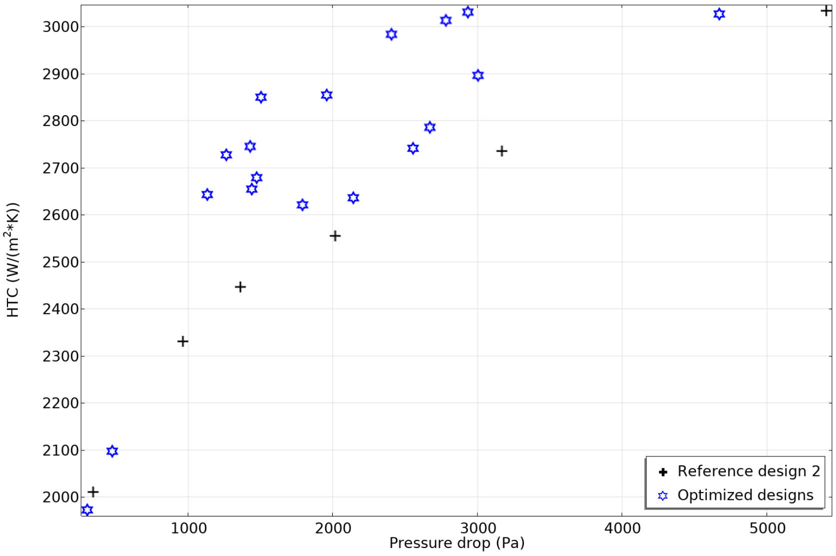

Figure D.1: Performance comparison of HTC against Δp for a set of optimized designs and reference design 2 on $Re = 300$